Materials Advances

ROYAL SOCIETY OF CHEMISTRY

PAPER

View Article Online
View Journal | View Issue

Cite this: *Mater. Adv.*, 2025, 6, 9678

Cameroonian natural clay derived Linde type LTA zeolite: demystifying and understanding the impact of the synthesis process on adsorption efficiency

Cyrille Ghislain Fotsop, Alexandra Lieb and Franziska Scheffler*

Herein, we reported on two approaches to understanding and demystifying the synthesis process of hierarchical zeolite LTA using cameroonian kaolin. Alkali fusion (AF) and metakaolinization (MK) are two separate techniques, which were used to optimize the synthesis of metakaolin. The derived zeolites were characterized by XRD, XRF, FESEM, FTIR and Raman spectroscopy, NMR, TGA and N_2 sorption analysis. Additional NaOH in the mixture of starting materials for the zeolite synthesis increased the relative crystallinity of the product to 92.10% and 94.71%, for both synthesis routes using metakaolin derived by MK and AF, respectively. Crystals with a cubic shape were visible in the SEM images, showing a full zeolitization. Metakaolin produced by AF was found to be most successful in the synthesis of LTA zeolite. CO_2 adsorption capacities of 3.96 and 3.53 mmol g^{-1}, were obtained using Z-AF-S1 and Z-MK-S1, respectively. The DSLSips model was found more suitable for the modelling of experimental data compared to DSL, DSLF, Freundlich and Langmuir models. The average isosteric heat of adsorption were 33.13 kJ mol^{-1} and 30.61 kJ mol^{-1} for the zeolite samples Z-AF-S1 and Z-MK-S1, respectively. The AF method was found to be a cost-effective and sustainable alternative approach for the production of commercial type 4A zeolite using natural cameroonian kaolin, involving a fast and low-cost chemical process.

Received 16th August 2025,
Accepted 28th October 2025

DOI: 10.1039/d5ma00915d

rsc.li/materials-advances

1. Introduction

The growth of anthropogenic emissions of carbon dioxide (CO_2), caused mostly by the combustion of fossil fuels, coals, and gases has become a significant environmental factor. Carbon dioxide is considered as the major cause of the greenhouse effect, which contributes to catastrophic weather changes and global warming,[1] with a contribution of about 60%. Based on such environmental issues, several studies have been performed in the field of elimination, storage, recycling and capture of carbon dioxide. Absorption processes are the most widely investigated techniques for the removal of post-combustion CO_2.[2] Commercial operations on CO_2 recovery based on absorption processes employing amines and organic compounds as adsorbent are still effective, but require more energy.[3] On the other hand, solid phase adsorption processes offer several advantages, due to their low energy consumption, their high selectivities in gas mixtures containing oxygen, methane and nitrogen[2] and the high regeneration capability of the materials in absorption–desorption cycles.[4] Consequently, several kinds of solid adsorbents, including activated carbons,[5] metal–organic frameworks,[6] silica gels[7] and zeolites[8,9] have been used. Notably, synthetic zeolites, especially those of type A and 13X, have been extensively investigated in CO_2 elimination technologies. Zeolite type A promote their suitability as adsorbent materials due to their particular properties such as low silica content, high porous structure, high chemical and thermal stability, eco-friendly characteristics and low cost.

Zeolites 4A are commonly synthesized using commercially available aluminosilicates. However, their synthesis is limited due to the high cost of reagents and other economic issues. Therefore, many researchers are interested in the usage of natural and lower cost reagents. A variety of minerals such as volcanic rocks,[10] kaolin[8,9] and halloysite[11] have been tested for the synthesis of zeolites. Kaolinite with its chemical composition $Si_2Al_2O_5(OH)_4$, high stoichiometric stability and SiO_2/Al_2O_3 ratio close to the aimed zeolite's, is relatively cheap and suitable for the synthesis of zeolite NaA.[12] Several publications have reported the synthesis of NaA type zeolite using kaolin as the primary aluminosilicate feedstock and alkaline ammonium, potassium and sodium hydroxide solutions[13,14] as starting materials. The reported synthesis procedures cover microwave-assisted,[15] one post fusion[16] and hydrothermal methods.[17] The transformation of kaolin to metakaolin, a more reactive and metastable phase, is essential for the synthesis of zeolites. Indeed, kaolin has a varying mineralogical

Otto-von-Guericke-University Magdeburg, Chemical Institute, Chair for Industrial Chemistry, Universitätsplatz 2, 39106, Magdeburg, Germany.
E-mail: franziska.scheffler@ovgu.de

composition and some impurities related to its original location. These impurities generally promote the formation of multiphase zeolites, when they are not completely dissolved. The alkali fusion procedure has the benefit of an improved metal dissolution in kaolin, quartz, aluminum and silica layers, when the mixture of sodium hydroxide and kaolin is performed in dry conditions compared to the metakaolinization procedure regarding the kaolin activation process.[18,19] Maia *et al.*[20] reported on the synthesis of zeolite NaA using Amazonian kaolin pretreated by alkali fusion, based on the variation of the Na/Al ratio (1.26, 1.36 and 1.45). Here a Na/Al ratio of 1.36 lead to zeolite NaA with the highest relative crystallinity.

Furthermore, Mezni *et al.*[21] optimized the synthesis parameters of zeolites NaX and NaA from Tunisian illite with a Si/Al molar ratio of 2, using metakaolinization and alkali fusion processes. In their studies, both processes were optimized to evaluate the optimal parameters. Zeolite NaA with a particle size ranging from 1.72 to 2.8 μm was achieved using a NaOH/illite mass ratio about 1.2 and a crystallization and aging time of 6 h and 24 h, respectively. Meanwhile, Wang *et al.*[9] reported on CO_2 adsorption through zeolite 4A obtained by hydrothermal synthesis from commercial kaolin. The textural properties of the obtained zeolite indicate a specific surface area of 13.372 $m^2\ g^{-1}$ with a micropore volume of 0.0011 $cm^3\ g^{-1}$. The synthesized zeolite 4A was found to be interesting for CO_2 adsorption with an adsorption capacity of 59.382 mL g^{-1}. Furthermore, Panda *et al.*[22] reported on the post-synthetic introduction of mesopores into the zeolite 4A for CO_2 adsorption. The achieved mesoporous zeolite material showed an enhanced specific surface area of 126 $m^2\ g^{-1}$, with a mesopore volume of 0.44 $cm^3\ g^{-1}$, compared to the initial one with a specific surface area of 39 $m^2\ g^{-1}$ and a mesopore volume of 0.13 $cm^3\ g^{-1}$. The CO_2 adsorption capacities were found to be 3.77 mmol g^{-1} and 3.41 mmol g^{-1} for the initial and mesoporous zeolite, respectively. On the other hand, the post-synthetic modification of zeolites with amines has been investigated. Regarding CO_2 adsorption, derivative materials are suitable promoting materials for CO_2 capture at low pressure, due to the interaction between different primary and secondary sites of amines and CO_2 molecules.[23–25] Simultaneously, the blockage of zeolite pores and CO_2 adsorption sites by amine molecules remains an issue for low pore volume zeolites such as zeolite 4A, which decreases the CO_2 adsorption capacity.[25] In addition, the choice of the adsorbent remains peremptory for selectivity and stability due to pressure fluctuations. Adsorption performance of zeolites are predicted using adsorption isotherm models. Several kinds of adsorption isotherm models are used to describe the adsorption equilibrium, usually isotherm models with a minimum of two parameters.[26] In general, the parameters of the isotherm models are used to evaluate the surface properties and affinity between the adsorbent and the gas molecules. Nonlinear regression has the advantage to improve the fit between isotherm models and experimental data.[27] At the same time, nonlinear regression proves to be a complex process and is known to be the best procedure to evaluate the isotherm variables at equilibrium.[3,28] Cameroonian kaolin, a clay rich in kaolinite, is attracting increasing interest thanks to the high quality of its deposits, which are found in various regions of the country, especially in the Center, West and on the Coast. Some areas, such as Mayouom, produce kaolin of a particularly high purity with a low content of sand and iron. These characteristics make it ideal for demanding industrial applications, such as the production of white ceramics, paper, paints and cosmetics. Recent research also suggests that high-whiteness calcined kaolin that meets international standards can be produced. At the same time, the country is exploring opportunities for locally processing and upgrading kaolin to create higher-value products. This versatile material has many applications in industry, cosmetics, agriculture and Crafts. It is also used in traditional beauty treatments, body masks and certain local remedies. However, its use in zeolite synthesis has not yet been fully explored in Cameroon. Nevertheless, this area represents significant potential for technological and industrial development. Developing this industry requires additional efforts in terms of infrastructure, processing, quality control and regulation, particularly to avoid the risks associated with uncontrolled use. The aim of this study is therefore to explore strategies for synthesizing zeolites from cameroonian kaolin. Cameroonian kaolin is a promising strategic resource for the local economy and the international industrial and cosmetic markets. Previous to our study, cameroonian clay was not yet explored regarding the field of zeolites for CO_2 adsorption, it was exploited for the development of absorbents for organic molecules.[29,30]

In this work, we report a new approach for the synthesis of zeolite NaA based on the optimization of the activation temperature for natural kaolin transformation and the assessment of the metakaolin obtained by alkali fusion and metakaolinization. The influence of crystallization time, temperature and sodium hydroxide concentration on the crystallinity of the synthesized zeolite A was investigated. The adsorption potential of cameroonian kaolin-derived zeolites as an adsorbent for CO_2 capture was explored. The effectiveness of Langmuir, Freundlich, Dual site Langmuir (DSL), Dual site Langmuir–Freundlich (DSLF) and Dual site Langmuir Sips (DSLSips) mathematical models on the prediction of adsorption capacity and error functions have been evaluated, in order to suggest the suitability of the model.

2. Experimental section

2.1. Chemicals and raw materials

2.1.1. Chemicals. The reagents used in this study were double distilled (dd) water, sodium hydroxide (NaOH, 98%, Sigma-Aldrich puriss p.a., Honeywell Fluka Fisher Scientific GmbH, Schwerte, Germany), sodium aluminum powder ($NaAlO_2$, technical grade, 98%, Sigma-Aldrich, St. Louis, USA), and kaolin which was harvested in Cameroon. $NaAlO_2$ was used to adjust the SiO_2/Al_2O_3 ratio during the synthesis. All chemicals were used without any further purification. For comparison with the XRD pattern of the synthesized zeolite A sample a commercial zeolite 4A (Köstrolith® 4AK, CWK, Bad Köstritz, Germany) was used.

2.1.2. Natural clay and geological localization. The raw kaolin used in the present work was collected in Kekem (West region, Cameroon) (Fig. S1). This area is a hilly plain landscape and constitutes the eastern extension of the Mbô plain.[31] The

Table 1 XRF analysis of raw kaolin and zeolite NaA

Sample		Metakaolin		Zeolite NaA	
Molar (%)	Kaolin	AF	MK	Z-MK-S1	Z-AF-S1
SiO_2	51.95	19.79	37.08	27.13	25.70
Al_2O_3	27.83	16.84	33.21	24.08	22.99
Na_2O	1.46	14.86	0.11	15.72	17.00
K_2O	1.26	0.10	0.16	0.06	0.22
MgO	0.27	0.001	0.001	0.001	0.08
CaO	0.31	0.036	0.03	0.02	0.03
TiO_2	1.99	0.675	1.16	0.75	0.29
MnO	0.01	0.00	0.00	0.00	0.00
$F_{e2}O_3$	1.70	0.384	0.68	0.45	0.37
H_2O	11.4	27.0	7.40	12.0	13.00
ZnO	0.03	0.002	0.005	0.00	0.001
ZrO_2	0.09	0.002	0.003	0.005	0.005
LOI	20.00	20.00	20.00	20.00	20.00
Total	100.04	99.76	100.03	100.21	99.89
SiO_2/Al_2O_3	—	—	—	2.02	1.99
Na/Al	—	—	—	1.01	1.10

microscopic organization of the different soil phases in this area indicates kaolin as the most abundant element and primary mineral, formed by the alteration of layers of several minerals by erosion, which are located mainly in lowland areas. Collected kaolin from this region contained in addition to kaolinite, illite, quartz and trace of metal oxides.[31] The chemical composition of Cameroonian kaolin is shown in (Table 1, Chapter 3.1.1).

2.2. Heat treatment and zeolite synthesis procedure

2.2.1. Heat treatment. Two thermal activation processes, namely alkali fusion (AF) and metakaolinization (MK), have been tested for the conversion of kaolin to metakaolin. In addition, the impact of calcination temperature, the addition of NaOH concentration and the effect of the additive of aluminum during the synthesis of zeolites were evaluated. The metakaolin used was optimized for the temperature ranging from 500–900 °C. For AF method, 10 g of NaOH was crushed in hand mortar and mixed with the amount of kaolin in the molar ratio 1/1 (kaolin/NaOH), for 60 min. The obtained solid mixture were placed in a ceramic crucible and fused by heating with the temperature ranging between 500–900 °C at the heating rate of 5 °C min^{-1} for 2 h. The obtained product after cooling was introduced in 100 mL dd water in polypropylene (PP) bottle and stirred for 6 h, then filtered, washed and dried at 70 °C overnight, the final product was noted AF. For MK method, the amount of kaolin was placed in a ceramic crucible followed by calcination in the same temperature range as those mentioned above. The final product after cooling was noted MK.

2.2.2. Synthesis procedure of zeolite NaA. Zeolite NaA was obtained by hydrothermal synthesis as following: 4 g of metakaolin obtained by AF or MK process was mixed with 3 M of NaOH, 25 g of dd water, 1 g of sodium aluminum to adjust the $SiO_2/A1_2O_3$ ratio. Afterwards, the initial gel mixture was stirred at 700 rpm for 4 h at 60 °C as gelification temperature in a water bath, the reaction mixture was transferred in a Teflon-lined autoclaves followed by crystallization step at 90 °C for 5 h. The obtained product was centrifuged at 3500 rpm for 15 min, washed with dd water four times until pH in the filtrate liquid was between 8 and 9 and dried at 100 °C overnight. Final product were coded Z-AF-S1 and Z-MK-S1 for AF and MK method respectively. Experimental procedure adopted in this work for the preparation of zeolite is given by (Fig. 1).

2.3. CO_2 adsorption study

Experimental CO_2 adsorption measurements were performed volumetrically using an automated ASAP 2020 gas sorption

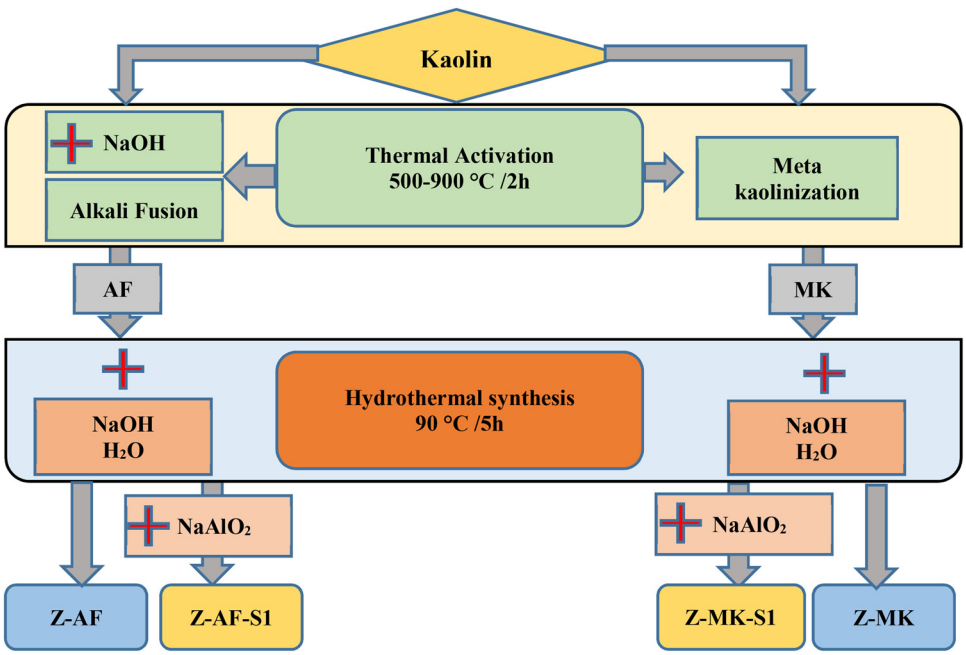

Fig. 1 Experimental procedure for the synthesis of zeolite NaA from kaolin.

system from Micromeritics GmbH, Norcross, USA. Before all experiments, approximately 50 mg of each sample was degassed under vacuum (10–5 mbar) at 350 °C for 10 h to remove all physiosorbed water molecules. Afterwards, the samples were cooled to each temperature of the experiment. CO_2 adsorption performance was evaluated at two temperatures (0 and 25 °C) for all samples over a pressure range of 0–1 bar. Volume changes were recorded continuously for each corresponding pressure value. The maximum adsorption capacities were evaluated at 1 bar for both temperature values for each sample.

2.4. Adsorption isotherm modelling

The experimental data were fitted to the Langmuir isotherm model, which is described by eqn (1).[3]

$$q_{eq} = \frac{q_{max} \cdot k \cdot p}{1 + k \cdot p} \quad (1)$$

where q_{eq} is the amount of CO_2 adsorbed at equilibrium (mmol g^{-1}), q_{max} is the maximum monolayer saturation capacity (mmol g^{-1}), k is the Langmuir constant and p is the pressure (bar).

Freundlich adsorption isotherm model describes a reversible multilayer adsorption. The mathematical expression is shown in eqn (2).

$$q_{eq} = K_f p^{1/n} \quad (2)$$

where q_{eq} is the amount of CO_2 adsorbed at equilibrium (mmol g^{-1}), K_f is the Freundlich constant, n is the heterogeneity factor and p is the pressure (bar).

The dual site Langmuir model (DSL) is based on the assumption that gas molecules are adsorbed on two different sites, the first site where chemisorption is the main mechanism and the second site where physisorption describes the main mechanism.[32] This model has the advantage of applying over a wide range of pressures. The DSL model is represented by eqn (3).[33]

$$q_{eq} = \frac{q_{max1} \cdot k_1 \cdot p}{1 + k_1 \cdot p} + \frac{q_{max2} \cdot k_2 \cdot p}{1 + k_2 \cdot p} \quad (3)$$

where q_{eq} is the amount of CO_2 adsorbed at equilibrium, q_{max1} and q_{max2} are the maximum saturation capacities of sites 1 and 2 (mmol g^{-1}), k_1 and k_2 are the Langmuir parameters (bar^{-1}) for sites 1 and 2 respectively, p is the pressure (bar).

The dual site Langmuir–Freundlich (DSLF) model (eqn (4)) and dual site Langmuir sips (DSLSips) (eqn (5))[34,35] were chosen to evaluate the accuracy of the adsorption behavior of CO_2 molecules towards adsorbates, assuming the existence of two heterogeneous adsorption sites in the adsorbates at different concentrations.[25] These models describe a better correlation of CO_2 adsorption over a wide range of pressure.[33] All parameters of these models are obtained by nonlinear fitting of experimental isotherms.

$$q_{eq} = \frac{q_{s1} \cdot k_1 \cdot p^{1/t_1}}{1 + k_1 \cdot p^{1/t_1}} + \frac{q_{s2} \cdot k_2 \cdot p^{1/t_2}}{1 + k_2 \cdot p^{1/t_2}} \quad (4)$$

$$q_{eq} = q_{max}\left(\frac{k_1 \cdot p}{1 + k_1 \cdot p} + \frac{(k_2 \cdot p)^t}{(1 + k_2 \cdot p)^t}\right) \quad (5)$$

where q_{s1} and q_{s2} are the maximum saturation capacities of sites 1 and 2 (mmol g^{-1}), t_1 and t_2 are the deviation from an ideal homogeneous surface of sites 1 and 2, k_1 and k_2 are the coefficients of sites 1 and 2 respectively; q_{max} is the maximum adsorption capacity (mmol g^{-1}), t is the heterogeneity factor and p is the pressure (bar).

2.5. Error function analysis

The average relative error and maximum relative error were determined to evaluate the accuracy of the adsorption isotherm fitting models in the operational adsorption pressure range. The average (Δq_{avg}) and maximum (Δq_{max}) relative error was calculated using the following eqn (6) and (7) respectively.[3]

$$\Delta q_{avg} = \frac{100}{n}\sum_{i=1}^{n}\left|\frac{q_{exp,i} - q_{cal,i}}{q_{exp,i}}\right| \quad (6)$$

$$\Delta q_{max} = \left|\frac{q_{exp,i} - q_{cal,i}}{q_{exp,i}}\right| \times 100 \quad (7)$$

where n represents the number of data points measured as a function of each temperature, q_{exp} and q_{cal} represent the experimental and calculated adsorbed amounts in moles respectively.

2.6. Characterization techniques

The structural identity of all samples was determined using X-ray diffraction (XRD) using an Empyrean powder diffractometer (PANanalytical, Almelo, The Netherlands) equipped with a Cu-tube (wavelengths $K_{\alpha1}$ = 1.540598 Å and $K_{\alpha2}$ = 1.544426 Å) operating at 40 mA and 40 kV. All samples were scanned from 4–90°2θ. The chemical composition of the raw kaolin was quantified using a Cubix-2300 X-ray fluorescence (XRF) spectrometer (Cubix-2300 model, PANanalytical, Limeil-Brévannes, France). The morphology and microstructure of all samples was recorded using a FEI SEM XL30 field emission scanning electron microscope (FEI, Hillsboro, USA) equipped with an energy dispersive X-ray spectrometer at an acceleration voltage of 20 kV. Fourier transform infrared spectroscopy (FT-IR) data was recorded using a Nicolet iS50 IR spectrometer (Thermo Scientific, Schwerte, Germany) in the 4000–200 cm^{-1} wavenumber range. Thermo gravimetric analysis (TGA) and differential scanning calorimetric (TGA-DSC) were carried out on a Netzsch STA 449C Jupiter (Netzsch, Selb, Germany) thermogravimetric analyzer. Raman analysis was performed with a LabRAM HR evolution (Horiba, Oberursel, Germany) using a monochromatic laser with a wavelength of 532 nm. Solid state ^{29}Si and ^{27}Al MAS NMR analyses were performed using a Bruker AVANCE II 400WB spectrometer (Bruker, Billerica, USA) with a frequency of 12 kHz. Dynamic vapor sorption was evaluated using an automatic vapor adsorption analyzer (DVS Vacuum, Surface Measurement Systems Ltd, England) at 20 °C and relative humidity ranging from 0 to 98%. N_2 sorption isotherms were recorded using a Micromeritics 3Flex instrument (Micromeritics, Norcross, USA). For the sorption analysis, all samples were first heated to 250 °C under vacuum and

then activated at 350 °C for 5 h under vacuum and the freespace was determined after each measurement with reactivated samples.

3. Results and discussion

3.1. Raw material characterization and compositional analysis

3.1.1. X-ray fluorescence (XRF) and X-ray diffraction (XRD). XRF analysis performed on kaolin and zeolite allowed to determine their chemical composition as well as the concentration of main elements present in these samples. These results are presented in (Table 1). The mass concentration of the major elements in the kaolin are 51.95% and 27.83%, representing SiO_2 and Al_2O_3 respectively with a SiO_2/Al_2O_3 ratio of approximately 1.97. This favors the synthesis of Na-A zeolite with the best ratio which should be close to 1, for the case of kaolin containing 100% by weight of kaolinite. Since the amount of Fe_2O_3 is less than 1.7% by weight of kaolin, the latter will be easily dissolved during alkali fusion. In the synthesised NaA zeolite, the amount of SiO_2 decreased considerably from 51.95% to 25.70% and 27.13% for Z-AF-S1 and Z-MK-S1, respectively comparable to the raw material, while the amount of Al_2O_3 is almost constant with the addition of sodium aluminate. This can be explained by the fact that during the formation of zeolite, only a necessary amount of these oxides is required for the nucleation phases. On the other hand, the amount of Na_2O increased significantly from 1.46% to 17.00% in the raw material and Z-AF-S1 sample. This increase is due to the addition of NaOH, during the heat treatment and the hydrothermal synthesis step; which enhances the nucleation and the kinetic growth of the zeolite.[36] Similarly, the Fe_2O_3 concentration decreased relatively from 1.70% to 0.37% and 0.45% for the zeolites Z-AF-S1 and Z-MK-S1 respectively. This decrease is related to the thermal treatment by alkali fusion, which facilitates the dissolution of impurities present in the kaolin compared to metakaolinization,[14,37] Similar observations were found for zeolite samples Z-MK and Z-AF obtained without the addition of sodium alumina (Table S1), zeolite Z-AF-900 and Z-MK-900 showed lower amounts of Al_2O_3 and SiO_2/Al_2O_3 ratios of 1.91 and 2.03 respectively, comparable to samples Z-AF-S1 and Z-MK-S1; this lower Al_2O_3 value could be due to a low concentration of sodium alumina or to the partial dilution of metakaolin, present in the synthesis gels. However, the addition of sodium aluminum improved the SiO_2/Al_2O_3 ratio to around 1.99.

The XRD patterns obtained for the raw kaolin and standard data base for chlorite, illite, kaolinite and quartz are shown in (Fig. 2), this shows the appearance of chlorite, illite, amorphous quartz phases, but mainly kaolinite characterized by peaks observed for angles 2θ = 6.16°, 12.32°, 18.56°, 24.84°, 31.19°, 34.59°, 35.14°, 40.90°, and 44.96°. Moreover, quartz is distinguished by the peaks observed for angles 2θ = 20.69° and 26.67°. These values are in agreement with the Joint Committee on Powder Diffraction Standards (JCPDS) database.[12] From this analysis, it is noted that the raw materials are mainly kaolinite and suitable for the synthesis of zeolites.

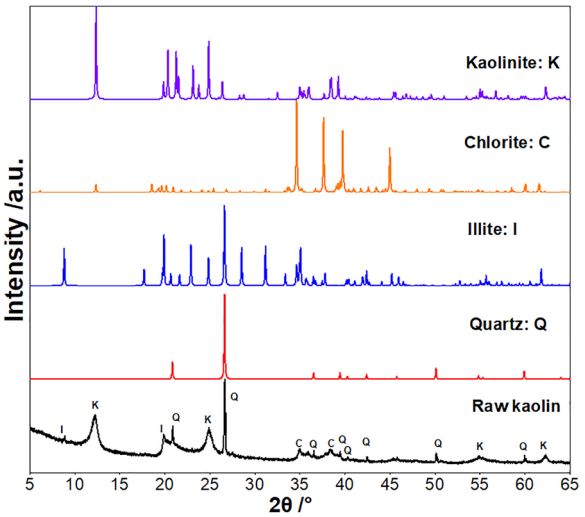

Fig. 2 XRD pattern of raw kaolin as well as those of illite, chloride kaolinite and quartz.

3.2. Synthesis optimization of zeolites from kaolin

3.2.1. The impact of thermal activation and phase transformation of kaolin. Metakaolin is more reactive and metastable than kaolin during the nucleation phases of zeolites.[38] We optimized the temperature during the thermal treatment, several dehydroxylation temperatures were used over a constant time. The XRD patterns of calcinated kaolin is shown in Fig. 3 for MK (a) and AF (b) method.

As can be seen from Fig. 3, thermal activation resulted in the transformation of the rigid crystalline structure of kaolin into a highly disordered and more amorphous structure due to the dehydroxylation process; visible by the disappearance of the standard peaks characteristic of kaolinite. The loss of mass during metakaolinization may be due to the destruction of the hydroxyl bonds linked to the different octahedral layers.[39] A quick comparison of the two heat treatment processes shows that for samples heated between 500–700 °C, it is almost impossible to destroy the characteristic peaks of the first reflection of kaolin. However, the increase in temperature causes the gradual disappearance of the typical kaolin phases, illite and chlorite, and favours the formation of metakaolin phases. The metakaolin phases consist mainly of nepheline, quartz and cristobalite ($NaAlSiO_4$) in the case of AF and sodium silicate (Na_2SiO_3) in the case of MK for the sample treated at 900 °C, which are easily soluble in alkaline solutions; the substances required for the preparation of zeolite 4A.[12] Above 900 °C, the tetrahedral sheets break up more easily and segregation of amorphous silica are observed, for the case of alkali fusion compared to metakaolinization. Samples obtained at this temperature show an optimal reactivity which can improve growth kinetics in agreement with previous reports,[40] 900 °C was chosen as optimal temperatures. Du *et al.*,[36] showed that dehydroxylation of kaolin is complete at 800 °C.

3.2.2. The impact of thermal activation on zeolite NaA synthesis. Fig. 4(a) and (b) shows the XRD patterns of zeolite synthesized from calcinated kaolin at different temperature of

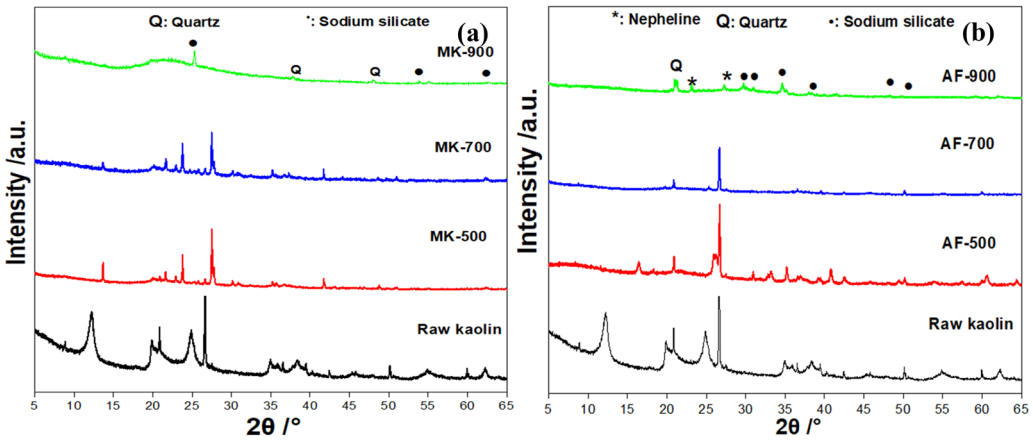

Fig. 3 XRD patterns of the sample after different activation temperature, where MK and AF are metakaolin obtained by metakaolinization (a) and alkali fusion (b), respectively.

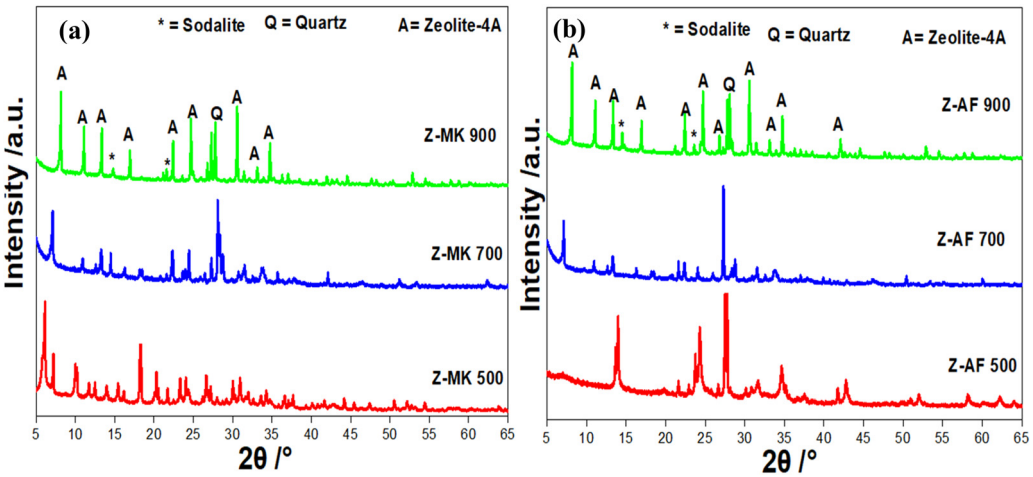

Fig. 4 XRD pattern of influence of thermal activation temperature on the synthesis of zeolite 4A, where Z-MK and Z-AF are zeolite obtained using metakaolinization (a) and alkali fusion (b), respectively.

dehydroxylation by alkali fusion and metakaolinization processes. XRD patterns of Z-AF-500, Z-AF-700, Z-MK-500 and Z-MK-700 samples show strong reflections characteristic of quartz at 2θ around 25–30° and few zeolite 4A phase with 2θ standard around 5–10°. Nevertheless, zeolite samples Z-AF-900 and Z-MK-900, show better phases characteristic of zeolite 4A, observable by 2θ = 7.23°, 10.21°, 12.89°, 16.20°, 22.31°, 24.51°, 29.39° and 34.56° comparable to Z-AF-500, Z-AF-700, Z-MK-500 and Z-MK-700, this difference in the XRD pattern may be explained by the partial conversion of kaolin to metakaolin during the heat treatment due to low temperatures and calcination times, previous work shows that, dehydroxylation of kaolin is beneficial at temperatures around 900 °C. This mean that, metakaolin is not yet in its amorphous phase. Additionally, the impurity phases present in kaolin are not totally dissolved. This could be explained by the appearance of other phases found, and therefore less reactive during the nucleation and growth step of the gel synthesis.[36] In addition, with temperatures higher than or equal to 900 °C, the samples obtained by AF method present mainly phases characteristic of zeolite A. Alkali fusion promoted the dissolution of metakaolin during the gelification step, and subsequent the formation of alumina-silica oligomers through the rearrangement of alumina and silica subunits. The samples obtained at 900 °C show a mixture of A, P and sodalite phases, but the majority of A phases for reflection peaks 2θ appearing between 6.72° and 12.6°, were assigned to reflections of zeolite A. Z-AF-900 and Z-MK-900 show additional sodalite phases characterized by the presence of peaks at 2θ = 14.23, 26°, Faujasite-Na appearing at 17.34° and NaP zeolite appearing at 21.22° for both zeolites, this observation could be due to the low amounts of sodium aluminate in the synthesis gels which decrease the crystal growth and favor the conversion of silica-alumina oligomers from crystalline nuclei to sodalite.[12,17] The presence of sodalite and NaP phases could be explained by the fact that the amount of aluminum present in the gel is not enough for the formation of pure phases of zeolite. On the other hand, it is observable that the amount of sodium silicate and sodium aluminum silicate present is not enough to enhance the growth of the crystallites, at the same time the whole portion of metakaolin was not been completely

converted to zeolite. It has been shown that the chemical reactivity of metakaolin increases with the calcination temperature.[41]

3.2.3. The impact of additive of aluminum source. Fig. 5 shows the impact of addition of sodium aluminate of the both metakaolin obtained at 900 °C using MK and AF method. As showing in this figure, the addition of sodium aluminate results in a significant appearance of the different pure phases of zeolite NaA for both metakaolin comparable to the commercial zeolite (Z–C), profiling maximum zeolitization of metakaolin obtained at 900 °C.[36] However, obtained samples by AF method (Z-AF-S1) showed the most crystalline phase and more intense peaks compared to Z-MK-S1 sample of the MK method. Lim *et al.*,[12] reported that alkali fusion improved the crystallinity of zeolite comparable to metakaolinization, which helped to understand that alkali fusion facilitated the formation of samples with high-crystallinity nuclei.[42] In addition, this could be explained by the maximum dissolution of impurities during alkaline fusion. The high mass attenuation coefficient of sodium increases the nucleation kinetics of growth gel, and enhances the efficient structuration of the tetrahedral of a three-dimensional network of $[SiO_4]^{-4}$ and $[AlO_4]^{-5}$, which allows them to have an open and regular microporous structure. Moreover, this addition also allows a better adjustment of the Si/Al ratio.[12] The relative crystallinity (RC) of zeolite was evaluated using eqn (8) below.[42] The purity phases of Linde type LTA zeolites were 92.1% for Z-MK-S1 and 94.71% for Z-AF-S1, comparable to the reference materials. Zeolite obtained using AF method was used for further investigation.

$$\%\,\text{Crystallinity} = \frac{\sum \text{of intensity of indidual peak of product}}{\sum \text{of intensity of indidual peak of standard zeolite}} \times 100 \quad (8)$$

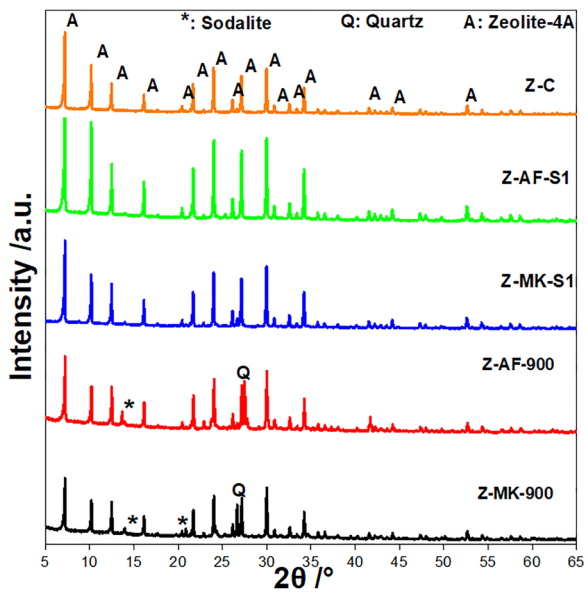

Fig. 5 XRD pattern of impact of additive of aluminum, where Z-MK-900 and Z-AF-900 are zeolite obtained without aluminum; Z-MK-S1 and Z-AF-S1 are zeolite obtained with aluminum respectively and Z-C is a commercial zeolite.

3.3. Optimization of factors during the nucleation of zeolites NaA

Different factors affecting the formation of zeolites NaA, including dosage of aluminum mass, sodium hydroxide concentration, time and temperature of crystallization were investigated in relation to obtained metakaolin by AF method.

The additive mass of aluminum have been adjusted from 0%, 25%, 50% and 75% by weight respect to AF/Al mass ratios. The XRD patterns are displayed in Fig. S2 in SI. The addition of a complementary aluminum to metakaolin, enhanced the transformation of sodium aluminum silicate during the gelation step, the conversion of the amorphous gel to crystalline nucleus and their growth.[36] Along with 0 wt% from a small amount of sodium aluminum, generates weak phases of Na-A zeolites and more amorphous phases. For amounts between 25% and 50% by weight, pure zeolite 4A phases are generated; characterized by standard reflection peaks. This shows that 50% of $NaAlO_2$ is enough to improve the nucleation kinetics and the formation of crystals with high crystallinity. It is also observed that higher SiO_2/Al_2O_3 ratios led to the formation of a mixture of unidentifiable A, X and other phases with a regular decrease in crystal size during the rearrangement phases, as in 75 wt% Saturation of $NaAlO_2$ decreased the nucleation of sodium hydroxyl and sodium silicate, which can be explained by the shifting of the characteristic peaks of zeolite NaA. This reveals that the formation is only successful with moderate SiO_2/Al_2O_3 values.[16]

Furthermore, the crystallization temperature were investigated at 70 °C, 80 °C, 90 °C, 100 °C and 110 °C. Fig. S3 shows the XRD pattern of the obtained samples. For the temperatures below 70 °C led to the formation of impure and more amorphous A phases with less characteristic zeolite NaA peaks. This can be explained by the low reaction rates during the crystallization steps and the rearrangement of the oligomers at the silica-alumina molecular scale, which makes it difficult to convert the amorphous gels into crystalline nuclei.[36] However, the increasing of crystallization temperature between 70–90 °C improve the crystallinity of the samples and the crystal growth respectively, especially for samples prepared at 90 °C, those result are in agreement with those report by Liu *et al.*[43] It is found that, this temperature value improved the growth of oligomers and nucleation of zeolites as well as the rate of formation of crystalline nuclei during gelation.[42] Meanwhile, higher temperature values (100–110 °C) led to the formation of phase mixtures, such as sodalite and P. A pure phase of the Linde LTA type is obtained at crystallization temperatures between 80 and 90 °C.

Additionally, crystallization time were monitored from 1 h to 24 h. The XRD pattern are presented in Fig. S4. Typical and more intense peaks of Linde type LTA zeolite can be observed for samples with crystallization times ranging from 5 h to 8 h. However, for longer times exceeding 10 h, A, X and Y phases are observed. This suggests that the crystallization of zeolite A was almost complete after 5 h, through a maximum nucleation of silica and alumina oligomers. However high times modified the crystal growth rate and the crystalline core; due to the non-stability of the zeolite structure when in an alkaline solution,

which is a consequence of the decrease of crystallinity. Ma *et al.*,[44] reported that the characteristic peaks of zeolite A disappeared at the expense of the formation of zeolite Na–X an Na–P, for high crystallization times.

Fig. S5 shows the XRD patterns of the effect of sodium hydroxide concentration from 2 M to 6 M. The formation of type A zeolite phases were found for NaOH concentration range between 3–4 M. The solubility of zeolite A improve with the increasing of hydroxide ion concentration. Indeed, the super-saturation in NaOH generated surface reactions between the monomeric anions of silicate and aluminate, which promoted the growth of microcrystals. However, higher alkalinity (6 M) generated a mixture of A, P and sodalite phases due to the maximum solubilization of the silica in the gel. This caused the over-saturation of the silicate and aluminate anions, resulting in the dissolution of zeolite A in the alkaline solution and its transformation into sodalite.[12,17] Tanaka *et al.*,[45] reported that optimal alkalinity reacted as a precursor of silica-alumina, thus promoting the transformation of A phase to sodalite. This study showed that 4 M NaOH was sufficient to obtain a highly crystalline zeolite.

4. Physico-chemical characterization of zeolite NaA

4.1. SEM and EDX analysis

SEM study was carried out to investigate the surface morphology. Fig. 6(a) and (b) shows SEM images and particle size distribution of Z-AF-S1 and Z-MK-S1 samples (Fig. 6c). The Z-AF-S1 and

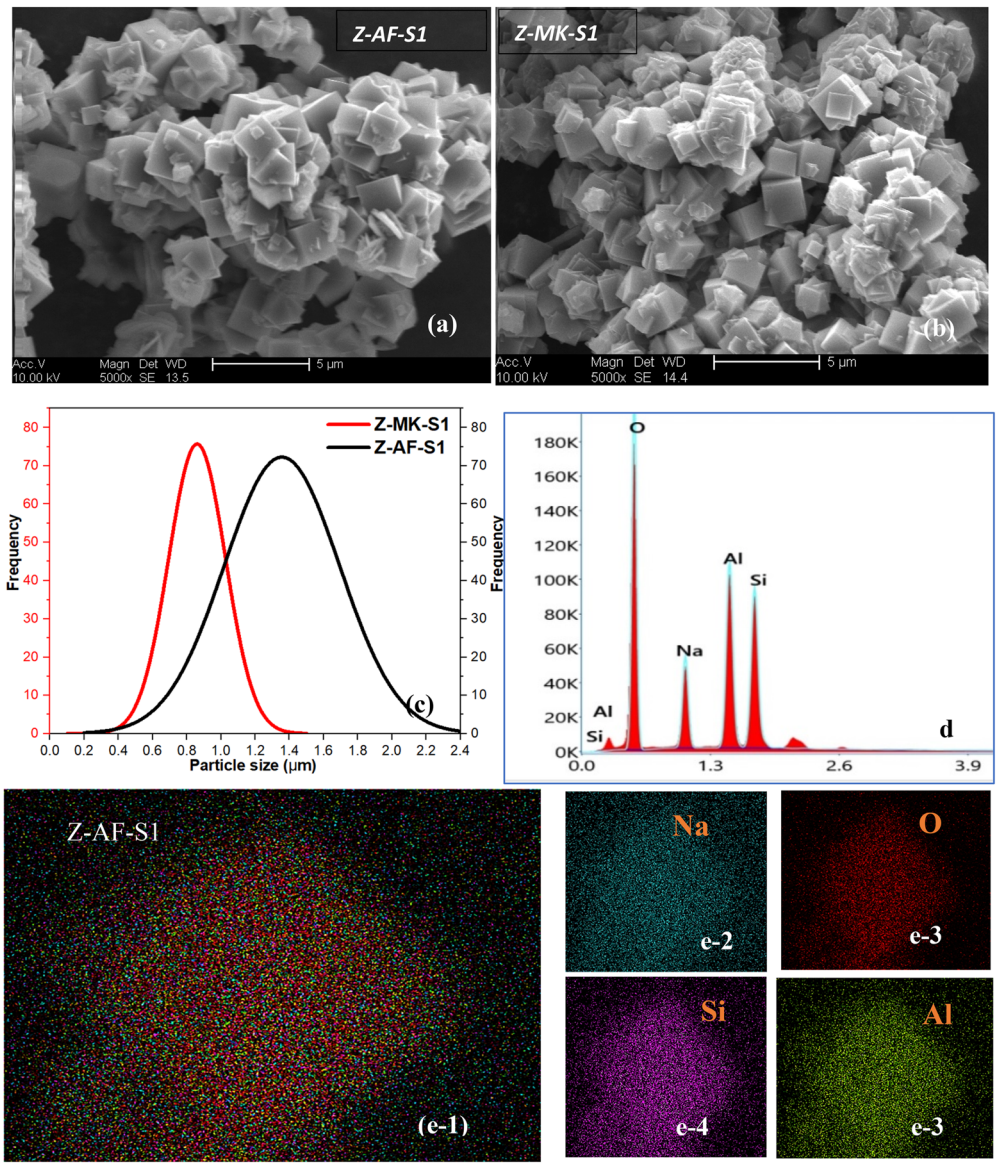

Fig. 6 FE-SEM images (a) and (b), particle size distribution (c) of zeolite Z-AF-S1 and Z-MK-S1, respectively. EDX spectra (d), EDX-mapping (e) and element distribution mapping of O, Na, Al and Si (from e-2 to e-5), respectively of synthesized Z-AF-S1 zeolite.

Z-MK-S1 samples showed similar morphologies identifiable by cubic crystals with homogenous size and an average particle size distribution of 1.35 μm and 0.86 μm, respectively. The cubic morphologies described a chamfered-edges crystals attributable to the typical shapes of Linde-type 4A zeolites.[46] However, smaller size of single crystals obtained by AF method have clearly defined particles; this shows that the addition of NaOH during the heat treatment increased the nucleation kinetics of the oligomers during the gelation and the maximum conversion of the amorphous gel into crystalline nuclei compared to MK method;[47] these results are in agreement with XRD pattern previous reported. This can be explained by a difference in the aluminum compensating ions in different synthesized zeolites. Furthermore, Z-MK-S1 shows the presence of unreacted metakaolin. Energy dispersive X-ray spectroscopy of Z-AF-S1 showed the presence of O, Na, Al, and Si atoms as presented in the spectrum (Fig. 6d).[48] EDX mapping (Fig. 6e), revealed a homogeneous distribution of all element present in the zeolite. Similar results were observed in the works reported by Wang *et al.*[9]

4.2. Fourier transform infrared (FT-IR) spectroscopy

FTIR spectrum of kaolin (Fig. 7a) shows elongation vibration bands of the Si–OH and Si–O units observable by absorption bands around 3650 cm^{-1} and 1075 cm^{-1}; bending vibration of the Si–O–Al and Al–OH units, characterized by absorption bands around 1659 cm^{-1}, 892 cm^{-1} attributable to stretching vibrations of physical water molecules. The strong bands at 455 cm^{-1} indicate the vibrations of the Si–O–Si bonds of the natural structure of the clay.[9,12] The disappearance of the Al–OH and Si–OH vibrational bands during the dehydroxylation phase shows that the bonds have been broken. On the other hand, the formation of metakaolin is materialized by the presence of new vibrational bands observable at 455 cm^{-1} and 892 cm^{-1}. Zhou *et al.*,[49] reported that the same bands were formed on metakaolin after the heat treatment. However, metakaolin AF exhibited a single vibrational band at 1495 cm^{-1} attributable to the antisymmetric stretching vibrations of T–O bonds (T = Al or Si) with aluminosilicate molecules between kaolin and NaOH compared to MK.

Fig. 7(b) shows the FTIR spectra of the samples Z-AF-S1 and Z-MK-S1. The symmetrical stretching vibration bands observable in the regions 335–495 cm^{-1}, 725–740 cm^{-1}, 515–590 cm^{-1} and 995–1005 cm^{-1} are attributable to the vibrational modes of the internal bonds of TO_4 (T= Al or Si), Si–O–Al, Si–O and Al–OH tetrahedral respectively. Somderam *et al.*,[40] reported that zeolites with the same IR spectra and structural groups belonged to the same Linde type LTA. Additionally, the presence of the bending bands of 4-chain rings of the Al–O and Si–O tetrahedron of sodalite are attributed with the vibration bands below 495 cm^{-1},[9,50] The overview highlights that, zeolite NaA was formed and having the same structural groups.

4.3. UV Raman spectroscopy

Fig. 8a shows the Raman spectra of zeolite samples, exhibiting high resolution bands characteristic of zeolite A at wavelengths of 270, 330, 397, 500, 645 and 670 cm^{-1}.[51] The Raman bands for wavelengths in the range 200–280 cm^{-1} are those proceeding from the eight-chain rings. Those between 300 and 370 cm^{-1} are attributable to the bending modes of the T–O–T (T = Si or AL) six-chain rings. In addition, the bands in the range 430–550 cm^{-1} are those with four-membered rings and attributable to the Si–O–Al ring.[52,53] This showed that zeolite A has been successfully synthesized and had 8, 6 and 4 chain rings, using AF or MK metakaolin with different secondary aluminum sources. Furthermore, the band appearing at 670 cm^{-1}, correspond to the T–O symmetric stretching mode (T = Si/Al). Indeed, zeolites with 4 pairs of altered –Si–O– members are those showing a strong Raman band above 600 cm^{-1}.[52,54] However, the band around 150 cm^{-1}, are attributable to the 8-membered rings of Si–O and Al–O present in the zeolite.

The thermal behavior of the synthesized zeolites represented in Fig. 8b displayed significant weight losses of 17.54% and 17.24% appearing at 155.01 °C and 154.24 °C which continues up to 300 °C for Z-AF-S1 and Z-MK-S1 respectively. The losses at 155.01 °C and 154.24 °C corresponded to the progressive elimination of externally adsorbed water molecules in the upper cages of the zeolite structure at low temperatures and physiosorbed water molecules in the sodalite cages at temperatures around 300 °C. This indicated the dehydration of the zeolite structure and the volatile compounds contained in the pores of zeolites.[47,60] Furthermore, the second exothermic peak appearing

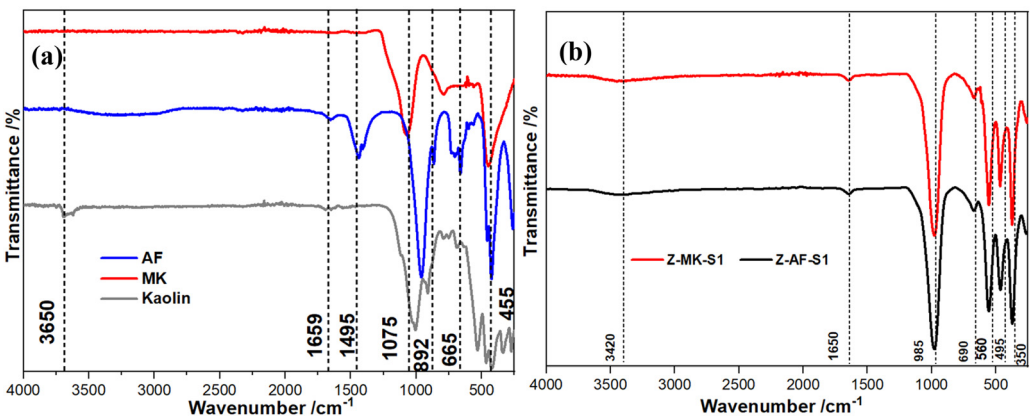

Fig. 7 FT-IR spectra of kaolin, metakaolin obtained by alkali fusion (AF) and metakaolinization (MK) (a) and synthesis Z-AF-S1 and Z-MK-S1 zeolite (b).

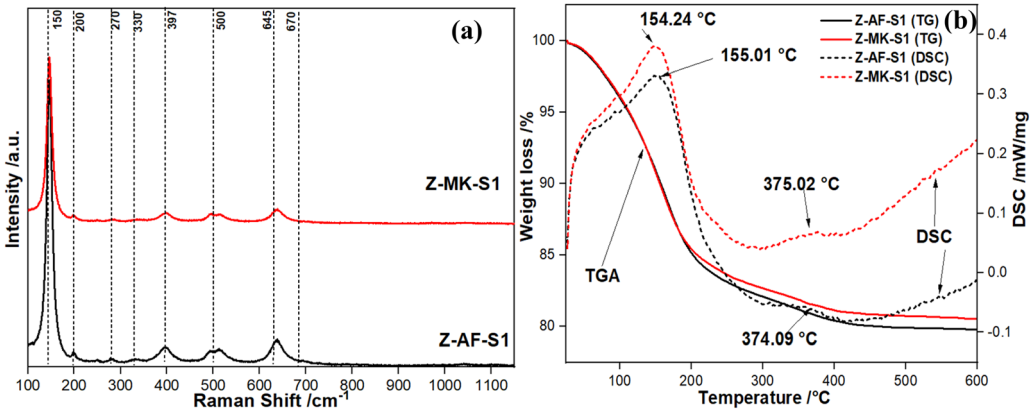

Fig. 8 Raman spectra (a) and TGA-DSC curves (b) for synthesis zeolite Z-AF-S1 and Z-MK-S1.

at 375 °C corresponded to the breakdown of the internal hydroxyl bonds of the zeolite structure.[42] It was found that both samples showed a continuous and almost constant weight loss up to 500 °C. Nevertheless, the zeolite samples obtained retained their high structural stability at high temperatures, highlighting characteristic properties of 4A zeolites.

4.4. Magic-angle spinning (MAS)-nuclear magnetic resonance (NMR)

The typical MAS-NMR ^{27}Al and ^{29}Si resonance spectra of the synthesized zeolite samples are presented in Fig. 9(a) and (b). The both samples showed a single resonance around 58.47 ppm and −89.68 ppm for MAS-NMR ^{27}Al (Fig. 9a) and MAS-NMR ^{29}Si (Fig. 9b) respectively. These two single resonance values correspond to the tetrahedral coordinated $Al(OSi)_4$ and $Si(OAl)_4$ species in the frameworks of the zeolite units. $Al(OSi)_4$ and $Si(OAl)_4$ are typical species of highly crystalline LTA zeolites. Wang *et al.*,[9] reported that Zeolite 4A showed a single resonance around 57.810 ppm and −92.017 ppm for MAS-NMR ^{27}Al and ^{29}Si respectively. This shows that aluminum from the dissolution of metakaolin in alkaline solution has shifted to four- and six-coordinate Si–O network to promote the formation of $Si(O–Al)_3(O–Si)$ framework during gelation exhibiting suitable lattices.[55] These observations indicate the presence of aluminum with a coordination number between Al(IV)–Al(VI), which facilitated their coordination with Si–O during zeolization step.

4.5. N_2 adsorption–desorption isotherms

Fig. 10(a) highlights the N_2 adsorption–desorption isotherms for synthesized zeolite Z-AF-S1 and Z-MK-S1. The samples Z-AF-S1 and Z-MK-S1 presented BET surface areas of 32.3 $m^2\ g^{-1}$ and 50.8 $m^2\ g^{-1}$, respectively (Table S2). Z-MK-S1 sample display a higher BET surface compared to Z-AF-S1 sample. Additionally, Fig. 10 showed a more visible hysteresis loop for Z-AF-S1 sample, indicating the presence of a mesoporous structure.[9] The N_2 adsorption–desorption isotherms obtained are of type IV according to the IUPAC classification.[56] The BET N_2 adsorption–desorption surface values obtained are close to those obtained in previous works 27.6 $m^2\ g^{-1}$ [57] 26.9 $m^2\ g^{-1}$ [9] and higher than 7.3 $m^2\ g^{-1}$ for commercial zeolite.[57] The difference in physicochemical properties may be attributed to the difference between the synthesis methods (AF and MK) and the variation of the chemical composition of kaolin compared to previous work. However, the difference with commercial zeolites is due to the variation of the Si/Al ratios and the presence of ion and binders in the pores of zeolites. Liu *et al.*,[58] reported that the access points of N_2 molecules in type 4A zeolites are partially blocked by ion present in their structure. This is

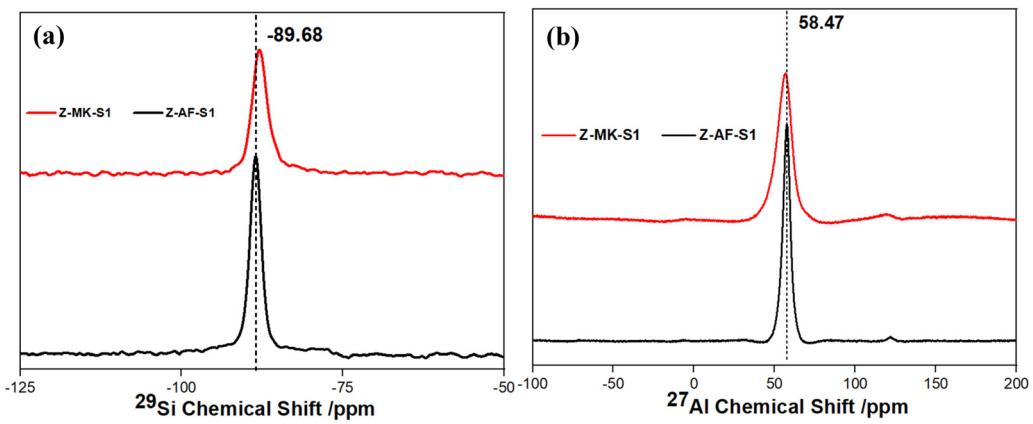

Fig. 9 Magic-angle spinning (MAS)-nuclear magnetic resonance (NMR) ^{27}Al (a) and ^{29}Si (b) spectra for synthesis zeolite Z-AF-S1 and Z-MK-S1.

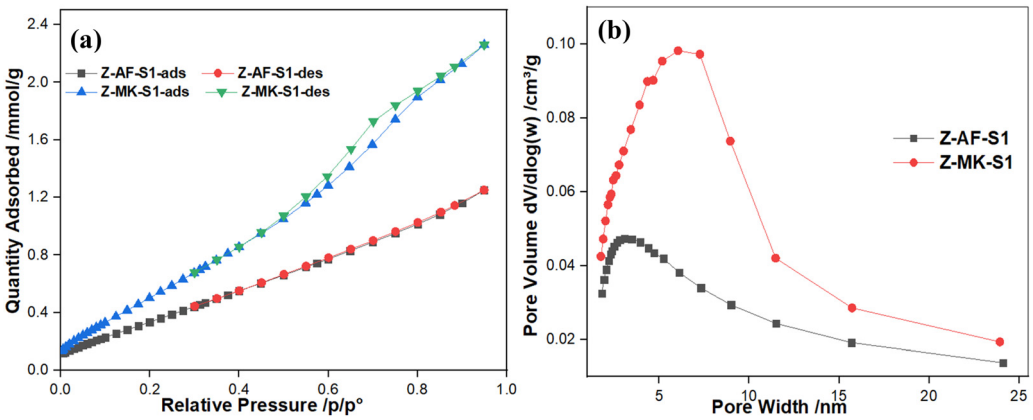

Fig. 10 N_2 adsorption–desorption isotherm (a) and BJH pore size distribution (b) of synthesized zeolite (Z-AF-S1 and Z-MK-S1).

reflected in low surface area values $< 30\ m^2\ g^{-1}$. Fig. 10(b) shows the pore width distribution of the both samples, using the Barrett–Joyner–Halenda (BJH) model; with an average pore width between 5–15 nm. Table S2 present the average micropore and total pore volume of the synthesized zeolite samples. The overall textural properties of the sample obtained by alkali fusion method indicate its high adsorption capacity and also suggest its application in CO_2 adsorption.[59] It should also be noted that the adsorption capacity of CO_2 is not only due to the textural properties but also to the presence of ion present in the zeolite structure. In addition, these ions in particular sodium provide supplementary active sites for the adsorption of CO_2.

5. CO_2 adsorption

5.1 CO_2 adsorption isotherm

CO2 adsorption on hierarchical zeolites Z-AF-S1 and Z-MK-S1 was performed by volumetry at 0 °C and 25 °C, over the relative pressure range of 0 to 1 bar. The adsorption isotherms obtained were very satisfactory with respect to the adsorption capacity of each sample. Both samples showed very similar isotherms to each other. Fig. S6 shows the adsorption isotherm for CO_2, type I according to the IUPAC classification.[56] At the same time the sample Z-AF-S1 shows the highest CO_2 adsorption capacity in high pressure range[8,61] comparable to the zeolite Z-MK-S1, due to the experimental methodology and the large values of mesopores. On the other hand, this may be due to the polarization and steric effect of CO_2 molecules on the zeolite surface.[25,62] However, the Z-AF-S1 zeolite showed an adsorption capacity of 3.963 mmol g^{-1} and 3.534 mmol g^{-1}; while the Z-MK-S1 zeolite showed an adsorption capacity of 3.442 mmol g^{-1} and 3.066 mmol g^{-1} at 0 °C and 25 °C respectively, at the highest pressure of 1 bar. The obtained CO_2 adsorption capacities are largely superior to those of commercial zeolite 2.47 mmol g^{-1} at 25 °C.[9,57] Aquino *et al.*,[63] reported on the synthesis of zeolites A and X using fly ash, the CO_2 adsorption capacity obtained was 1.37 mmol g^{-1} and 1.97 mmol g^{-1} for zeolites A and X respectively. The main difference may be due to the difference in the raw materials. In addition the variation in adsorption capacity could be elucidated by the difference in textural properties; furthermore, the high pore volumes, micropores, and BET surface area favor the diffusion of CO_2 molecules into the zeolite pores.[1,64] Additionally, the low CO_2 adsorption capacity with Z-MK-S1 comparable to Z-AF-S1 could be related to the presence of ions with higher charges than sodium, such as Ca, Mg and Fe. This observation is also supported by the XRF analyses. Indeed, the presence of those ions reduces the affinity of CO_2 during the adsorption.[63] This means that during metakaolinization those ions are partially dissolved. Nevertheless, the adsorption capacities of CO_2 with both materials are considered satisfactory, comparable to other materials reported in previous works.[65,66] This result shows the accuracy of the alkali fusion method, this method allows to increase the presence of sodium ions in the zeolite, due to the addition of NaOH during the thermal treatment. This indicates that the structures of the synthesized hierarchical zeolites 4A are well defined and reliable for large scale applications. Furthermore the raw kaolin is suitable for the preparation of hierarchical zeolite LTA. In addition, XRD pattern (Fig. S7) and FTIR spectra (Fig. S8) of Z-MK-S1 and Z-AF-S1 after CO_2 adsorption–desorption cycle, also show that the zeolite 4A obtained is promising for CO_2 adsorption cycle. These results emphasize the structural stability of zeolites during CO_2 adsorption. Moreover, the zeolite obtained retains its structural and physical properties after CO_2 desorption cycles.

The influence of adsorption temperature on CO_2 adsorption capacity was also investigated. Fig. S6 shows that the CO_2 adsorption capacity with both samples changes significantly with increasing temperature. It is evident that the increase in temperature promotes the drop in the adsorption capacity of these zeolites under the same pressure conditions, this observation suggests the physisorption behavior of the adsorbents.[22] In recent work, increasing the temperature from 0 °C to 25 °C resulted in a decrease of 18–30%; as well as a variation of 14.1–26.6%[63] in the adsorption capacity of CO_2. In this study, a change in temperature from 0 °C to 25 °C resulted in a 10% decrease in adsorption capacity for Z-AF-S1 zeolite and 11% for Z-MK-S1 zeolite. This indicates a significant decrease with temperature. This shows that high flue gas adsorption temperatures are not suitable for zeolites for CO_2 capture.[4] This significant change may be due to the breakdown of the Lewis basic sites formed by oxygen

Table 2 Adsorptison capacity of CO_2 on zeolite 4A

	Synthesis conditions				CO_2 adsorption				
Zeolite	Method	NaOH/weight ratio	Crys.[c] temp.[d] (°C)	Crys.[c] time (h)	Experimental apparatus	Pressure (bar)	Temp.[d] (°C)	Uptake (mmol g^{-1})	Ref.[e]
NaA	AF[a]	1.2	100	12	TGA	0.1	30	1.18	65
NaA	AF[a]	2	80	24	Volumetric	1	30	3.52	58
NaA	MK[b]	—	90	3.5	Volumetric	5	25	2.64	9
NaX	AF[a]	1.4	80	7	TGA	1	25	3.30	67
NaA	AF[a]	1	100	5	Fixed bed	0.05	20	0.56	68
NaA	AF[a]	1.4	90	4	Volumetric	1	25	2.07	57
NaA	AF[a]	1.2	95	8	TGA	1	50	2.39	63
							70	2.10	
							90	1.57	
NaA	AF[a]	1	90	5	Volumetric	1	0	**3.96**	This work
							25	**3.53**	
NaA	MK[b]	—	90	5	Volumetric	1	0	**3.44**	This work
							25	**3.06**	

[a] Alkali fusion (AF). [b] Metakaolinization (MK). [c] Crystallization (Crys.). [d] Temperature (Temp.). [e] Reference (Ref.).

atoms located on the surface of zeolite. Furthermore, low adsorption temperatures facilitate the presence of active basic centers and the strong interaction between CO_2 molecules and oxygen atoms in the tetrahedral and octahedral lattice located on the surface of the adsorbent.[25] Synthetic zeolites were also used for water vapor adsorption for the purpose of removing moisture. We evaluated the water vapor adsorption capacity of synthetic materials using gravimetric analysis at 20 °C and a relative humidity (RH) range of 0–98%. Fig. 10(a) and (b) shows the adsorption isotherms for Z-AF-S1 and Z-MK-S1. These curves demonstrate how the materials adsorb water vapor at different RH levels, showing monolayer and multilayer adsorption at low RH and capillary condensation at high RH. This shows that low temperatures are suitable for CO_2 removals from flue gases using zeolites. Table 2 summarizes the adsorption performance of some 4A zeolites derived from natural materials, considering the optimal synthesis conditions and adsorption operating performance.

5.2. Isotherm modeling

The experimental data were fitted with conventional Langmuir and Freundlich and hybrid Dual site Langmuir (DSL), Dual site Langmuir–Freundlich (DSLF) and Dual site Langmuir Sips (DSLSips) models. The set of parameters related to each isotherm model were determined to evaluate the degree of non-linear fit. The fit curves for the Z-AF-S1 and Z-MK-S1 samples are presented in Fig. 11(a) and (b); and the fit parameters are listed in Table S3. The adsorption isotherm curves for both zeolite samples, reveals a typical type I isotherm category according to the IUPAC classification characterizing monolayer adsorption with microporous adsorbents.[56] For both zeolite samples, the conventional Langmuir and Freundlich models do not show well-defined coefficients of correlation (R^2) (Fig. S9a and b) over the relative pressure range corresponding to each equilibrium temperature where monolayer and multilayer adsorption occurs. The Langmuir model, shows a process of continuous covering of the pores of the surface with respect to the enthalpy of adsorption and the heterogeneity of the surface.[69] On the other hand, the Freundlich isotherm based on the hypothesis that the adsorption energy at the adsorbent surface decreases reciprocally with the decrease of the adsorption sites, implies an infinite multilayer adsorption on heterogeneous surfaces.[69] Meanwhile the Langmuir model shows the best equilibrium adsorption capacity comparable to the

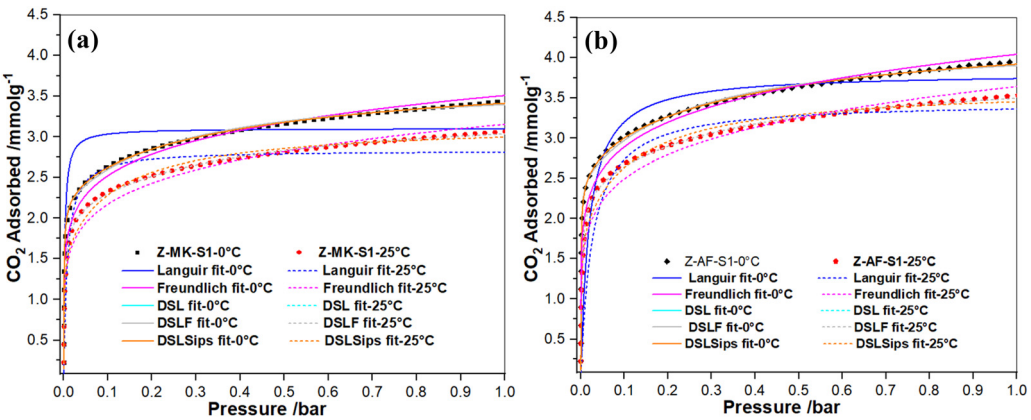

Fig. 11 Langmuir, Freundlich, dual site Langmuir (DSL), dual site Langmuir–Freundlich (DSLF) and dual site Langmuir sips (DSLSips) fitted of experimental data of CO_2 adsorption on Z-AF-S1 (a) and Z-MK-S1 (b) at equilibrium temperature.

Freundlich model, implying the presence of multilayer adsorption on the surface of zeolites. While the Freundlich model is unsuitable for equilibrium adsorption over the corresponding relative pressure range.

Instead, the DSL, DSLF and DSLSips models present better correlation coefficients of fit relatively higher than 0.99 (Fig. S9a and b), for both zeolite samples. However, the DSL model does not describe well the adsorption of mesoporous adsorbents comparable to the DSLF and DSLSips models. In addition, the DSL model assumes inhomogeneous surface coverage with respect to adsorption enthalpy, this model is based on monolayer adsorption and is recommended for micropore filling.[70] Indeed the majority of the adsorbents do not exhibit uniform interaction energies due to the non-homogeneity of the adsorbents.[69] The R^2 (Fig. S9a and b) values for the DSL model show a good fit between the experimental data and the nonlinear fitting model. In addition, this suggests the effective adsorption of CO_2 molecules in the multilayers of the adsorbent due to the high degree of surface heterogeneity.[71,72] In fact, the oxygen atoms located in the tetrahedral and octahedral networks present in the structure of the zeolites play the role of basic sites of Lewis; and they interact as receptors with the CO_2 molecules, due their symbiotic interactions between the adsorbents and the CO_2 molecules.[25]

However, the DSLF and DSLSips hybrid models have been used because of their extensional possibilities and their accuracy for multi-component mixtures. Furthermore, the DSLSips model is an alternative to overcome the deficits of the conventional Langmuir and Freundlich models;[73] this hybrid model is based on the premise that, adsorption occurs on monolayers and homogeneous surfaces; adsorption does not take into account interactions between adjacent sites and adsorbed gas molecules; gas molecules are adsorbed on well-localized and well-defined sites, with similar adsorption energies.[69,74] The R^2 values for this model show that CO_2 molecules are predominantly adsorbed in the molecular layers and pores of zeolites, due to the high level of heterogeneity of the surface. They consider a monolayer adsorption on homogenous surfaces with a filling of the micropores.

5.3. Isosteric heat (Q_{st}) of adsorption

The isosteric heat of adsorption (Q_{st}) was calculated using the Clausius–Clapeyron equation (eqn (9)) from experimental isotherm data recorded at 0 and 25 °C.[25,75]

$$\frac{Q_{st}}{RT^2} = \left[\frac{\partial(\ln P)}{\partial T}\right]_q \tag{9}$$

$$\ln P = -\left(\frac{Q_{st}}{R}\right)\frac{1}{T} + \frac{\Delta S}{R} \tag{10}$$

where ΔQ_{st} is the isosteric heat of adsorption, P is the relative pressure, T is the temperature and R is the gas constant. Based on two different temperatures and their isotherms; the Q_{st} value was obtained from the slope of the plot of ln(P) *versus* $1/T$ (eqn (10)). And the entropy change (ΔS) was determined using the intercept of equation (eqn (10)). The results are shown in Fig. 12(a) and (b). It is observable that for all samples, the isosteric heat decreases progressively with the increase of the adsorbed amount and the surface coverage. However, the change in entropy increases significantly with the amount adsorbed, which shows the energetic heterogeneity of the adsorption sites available on the surface of zeolites.[35] The average Q_{st} value were 33.128 kJ mol^{-1} and 30.607 kJ mol^{-1}, furthermore the change in entropy were 78.999 Jmol^{-1} K^{-1} and 90.778 Jmol^{-1} K^{-1} for zeolites Z-AF-S1 and Z-MK-S1, respectively. The Q_{st} and ΔS values obtained were close to those from the literature.[25,33] Panda *et al.*,[22] obtained a Q_{st} and ΔS value of 32.45 kJ mol^{-1} and 79.960 J mol^{-1} K^{-1} respectively. Notably, the derived Q_{st} value of zeolite Z-MK-S1 is slightly lower than those of zeolite Z-AF-S1. The high overall isosteric heat of adsorption for Z-AF-S1 can be explained by the strong interaction of Na^+ ions located in the α-cages and on the surface of the zeolite with the CO_2 molecules. Nevertheless, the lowers Q_{st} value shows that each obtained zeolite is easily regenerated after each adsorption cycle with low energy demand,[76] as observed in Fig. S7 and S8.

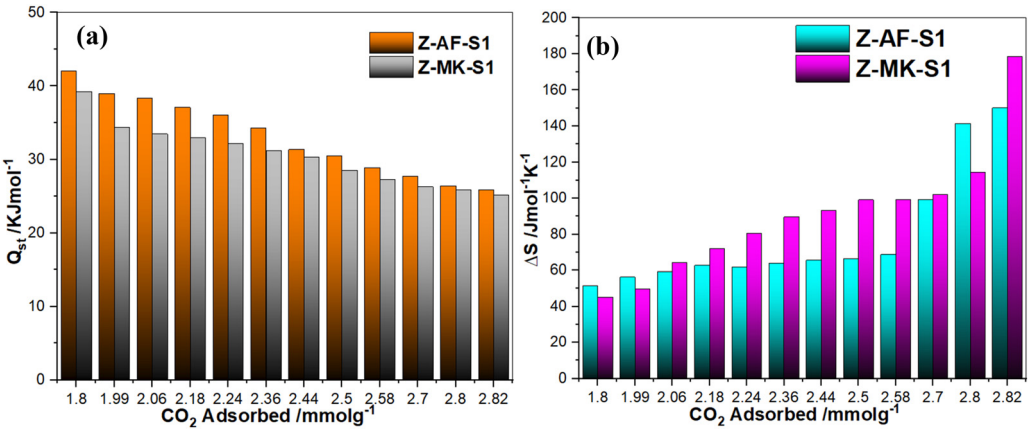

Fig. 12 Isosteric heat (Q_{st}) of adsorption (a) and change of entropy (b) of Z-AF-S1 and Z-MK-S1 zeolite.

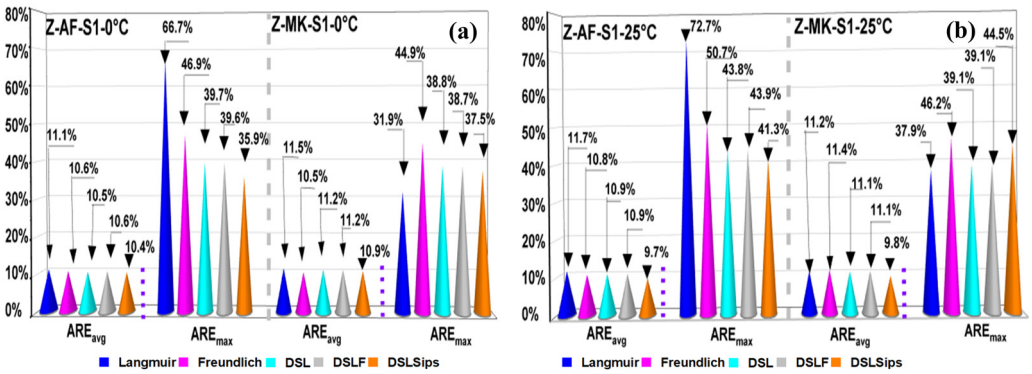

Fig. 13 Average (ARE_{vag}) and maximum (ARE_{max}) relative errors of the adsorption isotherm model for Z-AF-S1 and Z-MK-S1 at 0 °C (a) and 25 °C (b) respectively. The blue, magenta, cyan, gray and orange cones denote the Langmuir, Freundlich, dual site Langmuir (DSL), dual site Langmuir–Freundlich (DSLF) and dual site Langmuir Sips (DSLSips) isotherm models respectively.

5.4. Error analysis

The mean (Δq_{avg}) and maximum (Δq_{max}) relative error were calculated to evaluate the degree of adjustment of each adsorption isotherm model in the relative pressure range ($0 < P/P_0 < 1$). The results are presented in Fig. 13(a) and (b) for all isotherm models at 0 °C (a) and 25 °C (b). The Freundlich and Langmuir models presented the highest maximum and average relative errors comparable to the DSL, DSLF and DSLSips models over the corresponding relative pressure range at each adsorption equilibrium temperature; the variation between the Freundlich and Langmuir models was more significant, as observable by Fig. 13(a) and (b). This variation suggests the limitation of both adsorption isotherm models on the prediction of adsorption equilibrium characteristic of type I isotherms. The highest maximum relative error for the Freundlich and Langmuir models were 46.9% and 66.7% for adsorption at 0 °C; 50.7% and 72.7% for adsorption 25 °C for Z-AF-S1 sample. Furthermore, 44.9% and 31.9% for adsorption at 0 °C; 46.2% and 37.9% for adsorption at 25 °C for Z-MK-S1 sample respectively. This high variation can be explained by the low adsorption amount of CO_2 molecules. Meanwhile, the hybrid models DSL, DSLF and DSLSips are well consistent with the adsorption equilibrium data. In addition, the DSLSips model has the lowest values of the mean relative error, which assumes a small deviation between the measured isotherm data, and shows the spatial heterogeneity between the CO_2 molecules and the available adsorption locations on the surface of zeolites,[67] this model can more accurately predict the adsorption characteristics of mesoporous adsorbents.[70] It has the best precision in terms of the highest average and maximum relative errors and can be adopted to estimate the equilibrium adsorption capacity at an operating temperature over a well-defined relative pressure range.

6. Conclusion

In this work, Na-A zeolite samples were successfully synthesized using metakaolin derived from Cameroonian kaolin. The metakaolin used was derived from two methods namely alkali fusion and metakaolinization. The higher phase of the zeolites was achieved by optimizing the metakaolin derived from alkali fusion at 900 °C with a molar ratio NaOH/kaolin 1/1 using the hydrothermal process. The properties of the synthesized zeolites were compared with those of commercial zeolite. From the results obtained from the synthesis performed, it has been observed that the use of the formed metakaolin together with the addition of a secondary source of aluminum (sodium aluminate), with a concentration by weight of 50 wt% was successful to produce zeolite A. The obtained zeolite A exhibited a crystallinity of 82.1% and 89.6% with a crystallization temperature at 90 °C, a time of 5 h and NaOH concentration of 4 M to facilitate the formation of pure phase characteristic of Na-A zeolites. The properties of synthesized zeolite 4A have been characterized by numerous analytical techniques. The obtained samples showed good specific surface area, high thermal stability, and small crystallite size comparable to commercial zeolite. Zeolite produced by alkali fusion showed the most efficient CO_2 adsorption capacity at 0 °C and 25 °C, suggesting the strong presence of sodium ion in the structure of zeolite. The obtained zeolite samples are very attractive and can be used in gas separation processes, absorption of water vapors during drying processes and removal of pollutants from aqueous solutions. Cameroonian kaolin was found to be suitable for the synthesis of zeolite A as the material could be produced in high crystallinity without visible additional phases. DSLSips model was find more suitable to fit the experimental data compare to Freundlich and Langmuir models.

Author contributions

Cyrille Ghislain Fotsop: writing – original draft, visualization, validation, resources, methodology, investigation, formal analysis, data curation, conceptualization. Jakob Eggebrecht: characterization, investigation. Alexandra Lieb: Validation, supervision, investigation, formal analysis, conceptualization, data curation, writing – review & editing. Franziska Scheffler: validation, supervision, resources, funding acquisition, project administration, conceptualization.

Conflicts of interest

The authors declare no conflict of interest.

Data availability

Data will be made available on request.

Supplementary information (SI) is available. See DOI: https://doi.org/10.1039/d5ma00915d.

Acknowledgements

The authors thank the German Academic Exchange Service (DAAD) and the Graduate Scholarship Program of Saxony-Anhalt for funding. Additionally, the researchers acknowledge their gratitude to Dr-Ing. Markus Wilke and M. Sc. Karsten Harnisch for the assistance with the scanning electron microscope measurements, M. Sc. Jakob Eggebrecht (CWK, Bad Köstritz, Germany) for performing the RFA measurements, Ms Marlies Kupfernagel for her help with the TGA measurements and M. Sc. Elias Kluth for his help with the Raman spectroscopy

References

1 L. Hauchhum and P. Mahanta, CO_2 capture onto zeolite 13X and zeolite 4A by pressure swing adsorption in a fixed bed, *Appl. Mech. Mater*, 2014, 1456–1460, DOI: 10.4028/www.scientific.net/AMM.592-594.1456.

2 R. U. N. Foko, C. G. Fotsop, D. R. T. Tchuifon, C. Banenzoué and A. G. B. Azebaze, Green Synthesis of magnetic type Zeolites 4A as catalyst for the elimination of quinoline yellow by the Fenton process: Optimization and kinetic investigation, *Hybrid Adv.*, 2025, 100401.

3 J. Sren, U. Narkiewicz, A. W. Morawski, J. Wro and B. Michalkiewicz, Comparison of Optimized Isotherm Models and Error Functions for Carbon Dioxide Adsorption on Activated Carbon, *J. Chem. Eng. Data*, 2015, **60**(11), 3148–3158, DOI: 10.1021/acs.jced.5b00294.

4 Z. Zhang, Y. Xiao, B. Wang, Q. Sun and H. Liu, Waste is a misplayed resource: Synthesis of zeolites from fly ash for CO_2 capture, *Energy Procedia*, 2017, **114**, 2537–2544, DOI: 10.1016/j.egypro.2017.08.036.

5 H. Wei, S. Deng, B. Hu, Z. Chen, B. Wang and J. Huang, Granular Bamboo-Derived Activated Carbon for High CO_2 Adsorption: The Dominant Role of Narrow Micropores, *ChemSusChem*, 2012, **100084**, 2354–2360, DOI: 10.1002/cssc.201200570.

6 K. L. T. Nguena, C. G. Fotsop, A. Bopda, D. R. T. Tchuifon, F. H. K. Djioko, A. M. S. Ngueabouo, C. A. Madu, F. I. Ezema and E. E. Oguzie, Unraveling the sorption mechanism of industrial dyes onto Zr-based MOFs: computational and experimental modelling for highly efficient removal, *Mater. Adv.*, 2025, **6**, 579–597, DOI: 10.1039/D4MA00818A.

7 X. Xu, C. Song, B. G. Miller and A. W. Scaroni, Adsorption separation of carbon dioxide from flue gas of natural gas-fired boiler by a novel nanoporous b molecular basket Q adsorbent, *Fuel Process. Technol.*, 2005, **86**, 1457–1472, DOI: 10.1016/j.fuproc.2005.01.002.

8 C. Chen, D. Park and W. Ahn, Applied Surface Science CO2 capture using zeolite 13X prepared from bentonite, *Appl. Surf. Sci.*, 2014, **292**, 63–67, DOI: 10.1016/j.apsusc.2013.11.064.

9 W. Q. Sun, Y. Zhang and J. Cao, Synthesis of zeolite 4A from kaolin and its adsorption equilibrium of carbon dioxide, *Materials*, 2019, **12**, 9, DOI: 10.3390/ma12091536.

10 H. Ekene Mgbemere, I. C. Ekpe, G. Lawal, H. Ovri and A.-L. Chaudhary, Science & technology Preparation and Characterization of Zeolite type 4A using Kaolin from Ajebo, *J. Sci. Technol.*, 2019, **27**(4), 2427–2438.

11 T. F. Fanle, G. T. Kenda, D. R. T. Tchuifon, C. G. Fotsop, S. G. Fogang, I. K. Tchummegne and M. C. Kede, Design and characterisation of activated magnetic zeolite 4A from naturally occurring kaolin clay of Cameroonian origin for optimised dye removal by Fenton-like degradation, *Int. J. Environ. Anal. Chem.*, 2024, 1–29, DOI: 10.1080/03067319.2024.2389417.

12 C. G. Fotsop, A. Lieb and F. Scheffler, Tailoring the water vapor adsorption properties by thermal performance analysis of post-synthetically ion-exchanged LTA zeolite derived from Cameroonian kaolin, *J. Ind. Eng. Chem.*, 2025, DOI: 10.1016/j.jiec.2025.08.017.

13 F. H. Kamgang Djioko, C. G. Fotsop, G. Kamgang Youbi, S. C. Nwanonenyi, E. E. Oguzie and C. Ada Madu, Efficient removal of pharmaceutical contaminant in wastewater using low-cost zeolite 4A derived from kaolin: experimental and theoretical studies, *Mater. Chem. Phys.*, 2024, **315**, 128994, DOI: 10.1016/j.matchemphys.2024.128994.

14 M. Alkan, Ç. Hopa, Z. Yilmaz and H. Güler, The effect of alkali concentration and solid/liquid ratio on the hydrothermal synthesis of zeolite NaA from natural kaolinite, *Microporous Mesoporous Mater.*, 2005, **86**(1–3), 176–184, DOI: 10.1016/j.micromeso.2005.07.008.

15 S. Chandrasekhar and N. Pramada, Microwave assisted synthesis of zeolite A from metakaolin, *Microporous Mesoporous Mater.*, 2008, **108**, 152–161, DOI: 10.1016/j.micromeso.2007.04.003.

16 S. K. Kirdeciler and B. Akata, One pot fusion route for the synthesis of zeolite 4A using kaolin, *Adv. Powder Technol.*, 2020, **31**(10), 4336–4343, DOI: 10.1016/j.apt.2020.09.012.

17 S. H. Da Silva Filho, L. Bieseki, A. A. B. Maia, H. Treichel, R. S. Angelica and S. B. C. Pergher, Study on the NaOH/metakaolin ratio and crystallization time for zeolite a synthesis from kaolin using statistical design, *Mater. Res.*, 2017, **20**(3), 761–767, DOI: 10.1590/1980-5373-MR-2015-0631.

18 S. O. Otieno, F. O. Kengara, J. C. Kemmegne-Mbouguen, H. W. Langmi, C. B. O. Kowenje and R. Mokaya, The effects of metakaolinization and fused-metakaolinization on zeolites synthesized from quartz rich natural clays, *Microporous Mesoporous Mater.*, 2019, **290**, 109668, DOI: 10.1016/j.micromeso.2019.109668.

19 L. Ayele, J. Pérez-Pariente, Y. Chebude and I. Díaz, Conventional versus alkali fusion synthesis of zeolite A from low grade kaolin, *Appl. Clay Sci.*, 2016, 132–133, DOI: 10.1016/j.clay.2016.07.019.

20 A. A. B. Maia, R. S. Angélica and R. F. Neves, Use of industrial kaolin waste from the Brazilian Amazon region for synthesis of zeolite A, *Clay Miner.*, 2011, **46**(1), 127–136, DOI: 10.1180/claymin.2011.046.1.127.

21 M. Mezni, A. Hamzaoui, N. Hamdi and E. Srasra, Synthesis of zeolites from the low-grade Tunisian natural illite by two

different methods, *Appl. Clay Sci.*, 2011, **52**(3), 209–218, DOI: 10.1016/j.clay.2011.02.017.

22 C. G. Fotsop, A. Lieb and F. Scheffler, Core-Shell Material Based on Ion-Exchange-Assisted Growth of ZIFs on Chamfered-Edged Zeolite Crystals for N_2/CO_2 Adsorption: Modeling and Mechanism, *J. Environ. Chem. Eng*, 2025, **13**(6), 119887, DOI: 10.1016/j.jece.2025.119887.

23 Y. Fan and X. Jia, Progress in Amine-Functionalized Silica for CO_2 Capture: Important Roles of Support and Amine Structure, *Energy Fuels*, 2022, **36**(3), 1252–1270, DOI: 10.1021/acs.energyfuels.1c03788.

24 C. Li, X. Wang, A. Yang Chen, T. Zhao and F. Liu, Polyethyleneimine-Modi fi ed Amorphous Silica for the Selective Adsorption of CO_2/N_2 at High Temperatures, *ACS Omega*, 2021, **6**(51), 35389–35397, DOI: 10.1021/acsomega.1c04743.

25 D. Panda, E. A. Kumar and S. K. Singh, Amine Modi fi cation of Binder-Containing Zeolite 4A Bodies for Post- Combustion CO_2 Capture, *Ind. Eng. Chem. Res.*, 2019, **58**(13), 5301–5313, DOI: 10.1021/acs.iecr.8b03958.

26 J. P. N. Tejeogue, R. Djakba, C. G. Fotsop, N. Dobe, S. Mouhamadou, B. Wangmene and M. Harouna, Systematic metronidazole adsorption performance onto montmorillonite clay: Parametric study, process modelling and RSM optimisation, *Results Chem.*, 2025, **14**, 102153, DOI: 10.1016/j.rechem.2025.102153.

27 S. G. M. Mafo, D. R. T. Tchuifon, F. H. K. Djioko, A. N. Kouteu, C. G. Fotsop, S. D. M. Dongmo, G. Doungmo and N. G. Ndifor-Angwafor, Unravelling the efficiency removal of 2,4-dinitrophenol on coconut shell biomass-derived activated carbons theoretical and experimental investigation, *Biomass Conv. Bioref.*, 2025, **15**, 8821–8841, DOI: 10.1007/s13399-024-05663-6.

28 F. D. S. Feudjio, C. G. Fotsop, A. Bopda, D. R. T. Tchuifon, J. N. Ndi, R. A. Ntieche, H. M. Ngomo and M. Yılmaz, Tunable water vapor adsorption properties on ion exchange microporous zeolite Na-X derived from natural kaolin, *Inorg. Chem. Commun.*, 2025, **177**, 114379, DOI: 10.1016/j.inoche.2025.114379.

29 J. A. Mbey, F. Thomas, C. J. Ngally Sabouang and L. D. Njopwouo, An insight on the weakening of the interlayer bonds in a Cameroonian kaolinite through DMSO intercalation, *Appl. Clay Sci.*, 2013, **83–84**, 327–335, DOI: 10.1016/j.clay.2013.08.010.

30 G. Deffo, R. C. Tonleu Temgoua, S. Foukmeniok Mbokou, E. Njanja, I. Kenfack Tonlé and E. Ngameni, A sensitive voltammetric analysis and detection of Alizarin Red S onto a glassy carbon electrode modified by an organosmectite, *Sens. Int.*, 2021, **2**, 100126, DOI: 10.1016/j.sintl.2021.100126.

31 T. Paul, K. N. Aurelie, K. Lucas, N. J. Pierre and K. Véronique, Mineral and geochemical characterization of the weathering mantle derived from norites in Kekem (West Cameroon): evaluation of the related mineralization, *International Research Journal of Geology and Mining*, 2012, **2**(8), 230–242.

32 K. S. Sánchez-Zambra, *et al.*, CO_2 capture with mesoporous silicas modified with amines by double functionalization: Assessment of adsorption/desorption cycles, *Materials*, 2018, **11**, 6, DOI: 10.3390/ma11060887.

33 C. G. Fotsop, A. Lieb and F. Scheffler, Investigating the impact of heating rates on hydrothermal conversion of heat-treated kaolin into Linde-type LTA zeolite for water vapor sorption, *Mater. Adv.*, 2025, **6**(21), 8078–8091, DOI: 10.1039/D5MA00678C.

34 S. B. L. Ngomade, C. G. Fotsop, A. K. Bhonsle, N. Rawat, P. Gupta, R. Singh, I. K. Tchummegne, R. K. Singh and N. Atray, Pilot-scale optimization of enhanced biodiesel production from high FFA Podocarpus falcatus oil *via* simultaneous esterification and transesterification assisted by zirconia-supported ZSM-5, *Chem. Eng. Res. Des.*, 2024, **209**, 52–66, DOI: 10.1016/j.cherd.2024.07.031.

35 J. Peng, Y. Sun, Y. Wu, Z. Lv and Z. Li, Selectively Trapping Ethane from Ethylene on Metal−Organic Framework MIL-53(Al)-FA, *Ind. Eng. Chem. Res.*, 2019, **58**, 8290–8295, DOI: 10.1021/acs.iecr.9b00183.

36 F. Tchoumi, A. K. Tamo, G. Doungmo, C. G. Fotsop, J. C. Kemmegne-Mbouguen and E. Ngameni, Polymer-free nanocomposite from zeolite and acetylene carbon black as glassy carbon modifier platform for simultaneous electrochemical quantification of acetaminophen and caffeine, *J. Appl. Electrochem.*, 2024, DOI: 10.1007/s10800-024-02076-1.

37 L. Ayele, J. Pérez-Pariente, Y. Chebude and I. Díaz, Conventional versus alkali fusion synthesis of zeolite A from low grade kaolin, *Appl. Clay Sci.*, 2016, **132–133**, 485–490, DOI: 10.1016/j.clay.2016.07.019.

38 C. G. Fotsop, A. Lieb and F. Scheffler, Elucidation of the thermo-kinetics of the thermal decomposition of cameroonian kaolin: mechanism, thermodynamic study and identification of its by-products, *RSC Adv.*, 2025, **15**(39), 32172–32187, DOI: 10.1039/d5ra05149e.

39 I. Majchrzak-Kuceba and W. Nowak, A thermogravimetric study of the adsorption of CO2 on zeolites synthesized from fly ash, *Thermochim. Acta*, 2005, **437**(1–2), 67–74, DOI: 10.1016/j.tca.2005.06.003.

40 S. Somderam, A. S. Abd Aziz, A. H. Abdullah and R. Mat, Characterisation of NAA zeolite made from Malaysian kaolin, *Chem. Eng. Trans.*, 2019, **72**, 325–330, DOI: 10.3303/CET1972055.

41 K. L. T. Nguena, C. G. Fotsop, S. B. L. Ngomade, A. K. Tamo, C. A. Madu, F. I. Ezema and E. E. Oguzie, Mathematical modeling approach for the green synthesis of high-performance nanoporous zeolites Na-X optimized for water vapor sorption, *Mater. Today Commun.*, 2024, **37**, 107406, DOI: 10.1016/j.mtcomm.2023.107406.

42 C. G. Fotsop, A. Lieb and F. Scheffler, Insights into the synergistic effects of ZnO/MgO and Zn/Mg-modified porous zeolite as core-satellite materials for tuning water vapor sorption properties, *Appl. Surf. Sci. Adv.*, 2025, **30**, DOI: 10.1016/j.apsadv.2025.100855.

43 H. Liu, S. Peng, L. Shu, T. Chen, T. Bao and R. L. Frost, Magnetic zeolite NaA: Synthesis, characterization based on metakaolin and its application for the removal of Cu^{2+}, Pb^{2+}, *Chemosphere*, 2013, **91**(11), 1539–1546, DOI: 10.1016/j.chemosphere.2012.12.038.

44 Y. Ma, C. Yan, A. Alshameri, X. Qiu, C. Zhou and D. Li, Synthesis and characterization of 13X zeolite from low-grade natural kaolin, *Adv. Powder Technol.*, 2014, **25**(2), 495–499, DOI: **10.1016/j.apt.2013.08.002**.

45 H. Tanaka, Y. Sakai and R. Hino, Formation of Na-A and -X zeolites from waste solutions in conversion of coal – yash to zeolites, *Mater. Res. Bull.*, 2002, **37**(11), 1873–1884, DOI: **10.1016/S0025-5408(02)00861-9**.

46 T. Hu, W. Gao, X. Liu, Y. Zhang and C. Meng, Synthesis of zeolites Na-A and Na-X from tablet compressed and calcinated coal fly ash, *R. Soc. Open Sci.*, 2017, **4**(10), DOI: **10.1098/rsos.170921**.

47 Z. Wu, Preparation, characterization, and performance of 4A zeolite based on opal waste rock for removal of ammonium ion, *Adsorpt. Sci. Technol.*, 2018, **36**(9–10), 1700–1715, DOI: **10.1177/0263617418803012**.

48 M. I. Khan, K. Azizli, S. Su and Z. Man, Sodium silicate-free geopolymers as coating materials: Effects of Na/Al and water/solid ratios on adhesion strength, *Ceram. Int.*, 2015, **41**, 2794–2805, DOI: **10.1016/j.ceramint.2014.10.099**.

49 Z. Zhou, G. Jin, H. Liu, J. Wu and J. Mei, Crystallization mechanism of zeolite A from coal kaolin using a two-step method, *Appl. Clay Sci.*, 2014, **97–98**, 110–114, DOI: **10.1016/j.clay.2014.05.015**.

50 W. Mozgawa, M. Król, K. Barczyk and M. Science, FT-IR studies of zeolites from different structural groups, *Chemik*, 2011, **7**, 671–674.

51 Y. Yu, G. Xiong, C. Li and F.-S. Xiao, Characterization of aluminosilicate zeolites by UV Raman spectroscopy, *Microporous Mesoporous Mater.*, 2001, **46**(1), 23–34, DOI: **10.1016/S1387-1811(01)00271-2**.

52 B. Piriou and A. Navrotsky, A Raman spectroscopic study of glasses along the joins silica-calcium aluminate, silica-sodium aluminate, and silica-potassium aluminate, *Geochim. Cosmochim. Acta.*, 1982, **46**(11), 2021–2037, DOI: **10.1016/0016-7037(82)90182-X**.

53 Y. L. Tsai, *et al.*, Raman spectroscopic characteristics of zeolite group minerals, *Minerals*, 2021, **11**(2), 1–14, DOI: **10.3390/min11020167**.

54 P. Knops-Gerrits, D. E. DeVos, E. J. Feijen and A. Jacobs, Raman spectroscopy on zeolites, *Microporous Mater.*, 1997, **8**(1–2), 3–17, DOI: **10.1016/S0927-6513(96)00088-0**.

55 S. Su, H. Ma and X. Chuan, Hydrothermal synthesis of zeolite A from K-feldspar and its crystallization mechanism, *Adv. Powder Technol.*, 2015, **27**(1), 139–144, DOI: **10.1016/j.apt.2015.11.011**.

56 M. Thommes, *et al.*, Physisorption of gases with special reference to the evaluation of surface area and pore size distribution (IUPAC Technical Report), 2015, **87**, 1051–1069, DOI: **10.1515/pac-2014-1117**.

57 P. Wang, J. Cao, Y. Zhang and Q. Sun, Controllable Preparation of Cubic Zeolite A and Application of Langmuir Model in Carbon Dioxide Adsorption, *Nanomaterials*, 2021, **11**(12), 3375, DOI: **10.3390/nano11123375**.

58 L. Liu, R. Singh Xiao, A. Webley and Y. Zhai, Zeolite synthesis from waste fly ash and its application in CO_2 capture from flue gas streams, 2011, 795–800, DOI: **10.1007/s10450-011-9332-8**.

59 R. Morales, *et al.*, Assessment of the potential use of zeolites synthesized from power plant fly ash to capture – CO_2 under post – combustion scenario, *Adsorption*, 2020, **26**(7), 1153–1164, DOI: **10.1007/s10450-020-00245-0**.

60 E. Ghadamnan, S. R. Nabavi and M. Abbasi, NaLTA Zeolite in Water Softening Process: Synthesis, Characterization, Kinetic studies and process optimization by Response Surface Methodology (RSM), *J. Water Environ. Nanotechnol.*, 2019, **4**(2), 119–138, DOI: **10.22090/jwent.2019.02.004**.

61 T. H. Nguyen, S. Kim, M. Yoon and T. Bae, Hierarchical Zeolites with Amine-Functionalized Mesoporous Domains for Carbon Dioxide Capture, *ChemSusChem*, 2016, **9**(5), 455–461, DOI: **10.1002/cssc.201600004**.

62 J. Wang, R. Fu, S. Wen, P. Ning, M. H. Helal, M. A. Salem, B. B. Xu, Z. M. El-Bahy, M. Huang, Z. Guo, L. Huang and Q. Wang, Progress and current challenges for CO2 capture materials from ambient air, *Adv. Compos. Hybrid Mater.*, 2022, **5**, 2721–2759, DOI: **10.1007/s42114-022-00567-3**.

63 T. F. DeAqui, *et al.*, CO_2 adsorption capacity of zeolites synthesized from coal fly ashes, *Fuel*, 2020, **276**, 118143, DOI: **10.1016/j.fuel.2020.118143**.

64 J. B. Parra, C. O. Ania and S. Calero, Insights on the Anomalous Adsorption of Carbon Dioxide in LTA Zeolites, *J. Phys. Chem. C*, 2014, **118**(44), 25460–25467, DOI: **10.1021/jp507431c**.

65 W. Nowak, A thermogravimetric study of the adsorption of CO_2 on zeolites synthesized from flyash, *Thermochim. Acta*, 2005, **437**, 67–74, DOI: **10.1016/j.tca.2005.06.003**.

66 H. Yi, H. Deng, X. Tang, Q. Yu, X. Zhou and H. Liu, Adsorption equilibrium and kinetics for SO_2 CO_2 on zeolites FAU and LTA, *J. Hazard. Mater.*, 2012, **203–204**, 111–117, DOI: **10.1016/j.jhazmat.2011.11.091**.

67 G. Verrecchia, L. Cafiero, B. D. Caprariis, A. Dell'Era, I. Pettiti, R. Tuffi and M. Scarsella, Study of the parameters of zeolites synthesis from coal fly ash in order to optimize their CO_2 adsorption, *Fuel*, 2020, **276**, 118041, DOI: **10.1016/j.fuel.2020.118041**.

68 C. Lee, S. Park and S. Kim, Breakthrough analysis of carbon dioxide adsorption on zeolite synthesized from flyash, *Korean J. Chem. Eng.*, 2014, **31**(2), 179–187, DOI: **10.1007/s11814-013-0281-7**.

69 F. Raganati, M. Alfe, V. Gargiulo, R. Chirone and P. Ammendola, Isotherms and thermodynamics of CO_2 adsorption on a novel carbon-magnetite composite sorbent, *Chem. Eng. Res. Des.*, 2018, **134**, 540–552, DOI: **10.1016/j.cherd.2018.04.037**.

70 S. Woo, H. Lee, H. Ji and Y. Kim, Adsorption Isotherm Model for Analyzing the Adsorption Characteristics of Water Vapor to Commercially Available Silica Gel Adsorbents for Adsorption Desalination Applications, *J. Chem. Eng. Data*, 2021, **66**(2), 1144–1156, DOI: **10.1021/acs.jced.0c00927**.

71 V. K. Singh and E. A. Kumar, Measurement and analysis of adsorption isotherms of CO2 on activated carbon, *Appl. Therm. Eng.*, 2016, **97**, 77–86, DOI: **10.1016/j.applthermaleng.2015.10.052**.

72 S. Chowdhury and R. Balasubramanian, Holey graphene frameworks for highly selective post-combustion carbon capture, *Sci. Rep.*, 2016, **6**(1), 1–10, DOI: **10.1038/srep21537**.
73 V. J. Inglezakis, S. G. Poulopoulos and H. Kazemian, Insights into the S-shaped sorption isotherms and their dimensionless forms, *Microporous Mesoporous Mater.*, 2018, **272**, 166–176, DOI: **10.1016/j.micromeso.2018.06.026**.
74 M. A. Al-ghouti and D. A. Da, Guidelines for the use and interpretation of adsorption isotherm models: A review, *J. Hazard. Mater.*, 2020, **393**, 122383, DOI: **10.1016/j.jhazmat.2020.122383**.
75 T. S. Ramaprabhu, Integration of polymerized ionic liquid with graphene for enhanced CO_2 adsorption, *J. Mater. Chem. A*, 2014, **00**, 1–8, DOI: **10.1039/C4TA04808C**.
76 Y. Li, H. Yi, X. Tang, F. Li and Q. Yuan, Adsorption separation of CO_2/CH_4 gas mixture on the commercial zeolites at atmospheric pressure, *Chem. Eng. J.*, 2013, **229**, 50–56, DOI: **10.1016/j.cej.2013.05.101**.